PROGRESS REPORT

SUBMITTED TO: National Aeronautics and Space Administration
Langley Research Center
Hampton, Virginia 23665

INSTITUTION: Department of Physics
Hampton University
Hampton, Virginia 23668

TITLE OF RESEARCH: Direct Solar-Pumped Iodine Laser Amplifier

NASA GRANT NUMBER: NAG-1-441

PERIOD COVERED BY THIS REPORT: September 1, 1987 - February 29, 1988

PRINCIPAL INVESTIGATOR: Kwang S. Han

CO-PRINCIPAL INVESTIGATOR: In Heon Hwang

RESEARCH ASSOCIATES: Kyong Hon Kim
Larry V. Stock

CONTENTS

SUMMARY

The performed work in the research period from September 1, 1987, to February 29, 1988, can be divided into three categories. The first category includes the development of a XeCl laser pumped iodine laser oscillator which will be incorporated into the Master Oscillator Power Amplifier (MOPA) system. The developed XeCl laser produces output energy about 60 mJ per pulse. The pulse duration was about 10 nsec. When a 5 cm long laser tube filled with $t\text{-}C_4F_9I$ at the pressure 70 torr with the developed XeCl laser, a 100 μJ iodine laser output with pulse duration about 500 nsec was obtained. The research is continuing to increase the oscillator output energy to 1 mJ.

In the second category, the kinetic model for the solar-pumped iodine laser was refined and the algorithm for the calculation of a set of rate equations was improved to increase the accuracy and the efficiency of the calculation. The improved algorithm was applied to explain the existing experimental data taken from a flashlamp pumped iodine laser for three kinds of lasants, $i\text{-}C_3F_7I$, $n\text{-}C_4F_9I$, and $t\text{-}C_4F_9I$.

In the third category, various solid laser materials were evaluated for solar-pumping. The materials studied in this research were Nd:YAG, Nd:YLF and Cr:Nd:GSGG crystals. The slope efficiency of 0.17 percent was measured for the Nd:YLF near the threshold pump intensity which was 211 solar constants ($29W/cm^2$). The threshold pump intensity of the Nd:YAG was measured to be 236 solar constants ($32W/cm^2$) and the near-threshold slope efficiency was 0.12 percent. True CW laser operation of Cr:Nd:GSGG was possible only at pump intensities less than or equal to 1,500 solar constants ($203\ W/cm^2$). This fact was attributed to the high thermal focusing effect of the Cr:Nd:GSGG rod.

I. XeCl LASER PUMPED IODINE LASER OSCILLATOR

by In Heon Hwang

ABSTRACT

This report includes the development of a XeCl excimer laser pumped iodine laser oscillator which will be incorporated into the Master Oscillator Power Amplifier (MOPA) system. The developed XeCl laser produces output energy about 60 mJ per pulse. The pulse duration of the XeCl laser is about 20 nsec.

After filling 70 torr of t-C_4F_9I in a 5 cm long quartz cell with cross section 1 cm^2, the iodine laser tube was pumped with the XeCl laser longitudinally. The threshold pumping energy of the iodine laser oscillation was found to be about 20 mJ when the optical cavity was composed of a curved full reflector with radius of curvature 5 m and a 98.5 percent reflective flat output coupler mirror. The laser pulse duration from the iodine laser oscillator was measured to be 500 nsec.

INTRODUCTION

A solar pumped laser is an attractive laser system for space applications such as the laser propulsion of space vehicles in space and power transmission from space to Earth. The solar pumped laser can also be a primary power source on a different planet in the solar system when the planet is subject to exploration by human beings. Among the laser operation modes, a continuous wave (CW) mode of operation has apparently the best space applicability. However, in a specific application such as the laser propulsion of space vehicles, pulse laser also has good applicability [1].

At present, various experimental and theoretical research results are reported from various research institutions. The output power of the most powerful solar pumped CW laser reported at present reaches to about 60 W by using a solid state laser material (Nd: YAG) [2]. The experimental CW solar pumped gas laser research is conducted exclusively in the NASA Langley Research Center using iodine compounds. The output power of the solar simulator pumped gas laser reaches more than 10 W when n-C_3F_7I is used as the gas medium [3].

The solid state laser material has a couple of advantages such as a broad absorption band and a high active atomic density compared with the gaseous laser material, however, it has serious disadvantages for the solar-pumped laser application such as the thermal lensing and self-focusing effect when operated at a high power. Thus, the scalability is very limited. In constrast to the solid state laser material, the gaseous laser material does not have any self-focusing problem, and the heat removal from the laser material is very easily accomplished by circulating the laser gas.

The CW solar-pumped laser research is partially successful in various laboratories, however, because of the limitations of laser material and the weak solar irradiance, a single laser oscillator can hardly produce very high output pwoer. The projection to get 1 MW output power shows that the tube length of the laser oscillator should be about 10 m and the diameter about 2 m [4]. The laser optics for such a large laser system will be very heavy and the alignment of the laser optics will be very critical.

Introducing a Master Oscillator Power Amplifier (MOPA) system, the heavy laser optics can be eliminated and the degree of accuracy in the alignment of

the laser system can be reduced. Moreover, when a short pulse generating laser oscillator is incorporated with the amplifier, high peak output power could be achieved rather easily with a small amplifier. The calculation shows that a peak output power of 36 MW can be obtained with an amplifier that is 10 m in length and has a diameter of 10 cm when 2 torr of $i\text{-}C_3F_7I$ is filled in the amplifier and pumped with 200 solar constants [5]. To verify the MOPA concept, a XeCl excimer laser pumped iodine laser oscillator is developed in this research period as described in the following sections.

XeCl EXCIMER LASER

A XeCl excimer laser was developed in this research period to provide a high repetition rate pumping of the iodine laser oscillator. Generally, an excimer laser can provide a higher pumping rate than a flashlamp.

The schematic diagram for the electrical system for the excimer laser is shown in figure 1. The high voltage power supply (Candela Model HVD-1000A) can charge the energy storage capacitor (0.03 μF) up to 40 kV. When the spark gap switch is closed, the stored electrical energy in the capacitor is dumped into the laser head. Just prior to the main discharge between the laser electrodes (about 50 nsec prior to the main discharge), the spark arrays located along the cathode spark through the small capacitors (500 pF/each, 34 capacitors) [6]. The UV light from the spark arrays preionizes the laser gas between the main electrodes. The preionization is indispensable for the uniform glow discharge of the laser gas. It is now generally accepted that the preionized electron density in the laser volume must be over about $10^7/cm^3$ to achieve the uniform glow discharge in the excimer laser gas [7].

The laser discharge electrodes and spark arrays are housed in a laser chamber made of Pyrex glass tube. The inner diameter of the Pyrex tube is 10 cm and the length is 66 cm. The electrodes are separated 2 cm away and the discharge length is about 44 cm. The laser beam pattern from the excimer laser is approximately rectangular with sides 1 cm and 2 cm.

The gas handling system for the XeCl laser is shown in figure 2. The pressure inside the laser chamber was controlled by adjusting the three different gas ratios. Helium was used as the buffer gas in this experiment. The optimum mixing ratio of the gases is found to be 0.2 percent HCl;

7 percent Xe; 92.8 percent He when the total pressure is 1300 torr (25 psi) and the energy storage capacitor is charged to 30 kV.

The discharge current is measured with a current transformer (Pearson Electonics, Model 110). A typical current shape and the laser pulse shape are shown in figure 3. The peak current measured was about 2.5 k^A when the energy storage capacitor was charged to 30 kV. The lasing starts at the peak of discharge current and lasts about 10 nsec. The laser pulse shape was detected by a pyroelectric detector (Molectron P5-01) and the laser energy was measured by an energy meter (Scientech 36-2002 Power and Energy indicator, 36-0001 Disc Calorimeter). The output energy from the XeCl laser was 60 mJ/pulse when the energy storage capacitor was charged to 30 KV and the gas pressure inside the laser chamber was 1300 torr with optimum mixture ratio.

The optical resonator is composed of a full reflector with radius of curvature 5 m and a flat output coupler with a reflectance of 30 percent. All the mirrors are coated with dielectric outside so that the optical coating would not be damaged by the discharge product during the laser discharge. The reflectance of the output coupler is not optimized.

IODINE LASER OSCILLATOR

A 5 cm long quartz tube with 1 cm^2 square cross section was used as the iodine laser tube. The schematic diagram of the iodine laser is shown in figure 4. The pumping of the iodine lasant is accomplished by irradiating the laser tube with the XeCl laser light through the full reflector of the iodine laser. This full reflector is dielectric coated to have high reflectance for iodine laser line (1.315 μm) but highly transparent for XeCl laser line (308 nm) with radius of curvature 5 m. The output coupler of the iodine laser is a 98.5 percent reflective flat mirror.

The lasant used in this experiment is t-C_4F_9I. The vapor pressure of this compound is measured about 70 torr at room temperature (23°C). The absorption cross section of the t-C_4F_9I is $4.43 \times 10^{-19} cm^2$ at the wavelength of the XeCl laser (308 nm) [8]. This value is nearly three times larger than that of n-C_3F_7I ($1.2 \times 10^{-19} cm^2$) or i-C_3F_7I ($1.53 \times 10^{-19} cm^2$).

When the laser tube was filled with t-C_4F_9I at 70 torr and pumped by the XeCl laser light with energy 50 mJ, the iodine laser output was measured to be about 100 μJ. The laser energy output was measured by an energy meter and the

laser pulse was detected by a germanium photodiode (Judson J16-LD). The FWHM of the laser pulse was about 500 nsec as shown in figure 5. The current pulse of the XeCl laser discharge was used as the trigger source of the oscilloscope.

The threshold pumping energy for the iodine laser was found to be about 20 mJ. With this threshold energy the excited atomic iodine density can be calculated as follow. The rate equation for the exicted atomic iodine density is given as

$$\frac{dN^*}{dt} = WpN \qquad (1)$$

where Wp is the pumping rate, N* is the density of the excited atomic iodine and N is the density of t-C_4F_9I. In the equation (1), only pumping term is considered because the decay time of the excited state atomic iodine is very long compared with the pumping pulse time scale and the excited atomic iodine does not combine fast with radical (t-C_4F_9) to the original molecule.

The pumping rate is given as

$$Wp = \sigma_a F \qquad (2)$$

where σ_a is the absorption cross section of the t-C_4F_9I molecule at the wavelength of the XeCl laser and F is the photon flux (# of photons/cm^2 sec). In equation (2), the quantum yield of the t-C_4F_9i is assumed to be unity at the wavelength of 308 nm. If the absorbing medium is optically thin such that the photon flux does not change so much, then the equation (2) can be used in equation (1) to calculate the excited atomic iodine density. However, if the absorbing medium is optically thick, then the pumping rate has to be changed to spatial averaged form as

$$\langle Wp \rangle = \frac{1}{\ell} \sigma_a \int_0^{\ell} F(x)\, dx \qquad (3)$$

where ℓ is the length of absorbing medium.

The t-C_4F_9I gas is an optically thick medium thus the expression of equation (3) is adequate for the calculation of the excited atomic iodine density expecially when the pumping is accomplished longitudinally.

The photon flux is reduced by the Beer's law as the excimer laser beam propagates through the t-C_4F_9I gas in the following manner

$$F(x) = Foe^{-\sigma_a Nx} \tag{4}$$

where Fo is the incident photon flux and x is the propagated length. Substituting equation (4) into equation (3), the spatial averaged pumping rate is given as

$$\langle Wp \rangle = \frac{Fo}{\ell N}\left[1 - e^{-\sigma_a N\ell}\right] \tag{5}$$

Substituting equation (5) into equation (1) and if we assume that the pumping pulse is square-top pulse with duration 10 nsec and the threshold pumping energy is 20 mJ, the excited atomic iodine density is calcualted to be $N^* = 6.15 \times 10^{15}/cm^3$.

On the other hand, the threshold population density can be calculated from the laser threshold condition,

$$R_1 R_2 e^{2\sigma \Delta N\ell} = 1 \tag{6}$$

where R_1 and R_2 are the reflectances of the optical resonator, σ is the stimulated emission cross section of the excited atomic iodine, ΔN is the population inversion density and ℓ is the length of the t-C_4F_9I gas cell. Assuming $\sigma = 1 \times 10^{-18} cm^2$, the threshold population inversion density is calculated to be $\Delta N = 2.52 \times 10^{15}/cm^3$ when the pressure inside the gas cell is 70 torr. Those two results are well agreed within factor of 3. Comparing with the result of the threshold pump energy published by E. Fill et al., at Max Planck Institute with i-C_3F_7I [9], the threshold pump energy for t-C_4F_9I is only about one tenth of that of i-C_3F_7I.

REFERENCES

[1]. R. J. Glumb and H. Krier, J. Spacecraft 21, 70, (1984).

[2]. M. Weksler and J. Schwartz, SPIE, vol. 736 (1987), p. 84.

[3]. J. H. Lee, M. H. Lee and W. R. Weaver, Proceedings of the International Conference on Lasers '86, R. W. McMillan ed., STS Press, McLean VA (1987), p. 150.

[4]. R. J. De Young, G. H. Walker, M. D. Williams, G. L. Schuster, and E. J. Conway, NASA Technical Memorandum 4002 (1987).

[5]. K. S. Han, I. H. Hwang and Larry V. Stock, NASA Research Proposal NAG-1-441 (1988).

[6]. A. J. Kearsley, A. J. Andrews, and C. E. Webb, Optics Comm. 31, 181 (1979).

[7]. R. S. Taylor, Appl. Physics B 41, 1 (1986).

[8]. J. K. G. Krug and K. J. Witte, Max Planck Institute Report MPQ 61 (1982).

[9]. E. Fill, W. Skrlac and K. J. Witte, Optics Comm, 37, 123 (1981).

FIGURE CAPTIONS

Fig. 1. Electrical circuit for XeCl laser.

Fig. 2. Gas handling system of XeCl laser.

Fig. 3. A typical current shape of XeCl laser discharge and the laser pulse shape.

Fig. 4. Schematic diagram of iodine laser oscillator.

Fig. 5. Temporal characteristics of iodine laser output. The iodine laser output is delayed about 1usec from the XeCl laser pulse.

Fig. 1. Electrical circuit for XeCl laser.

Fig. 2. Gas handling system of XeCl laser.

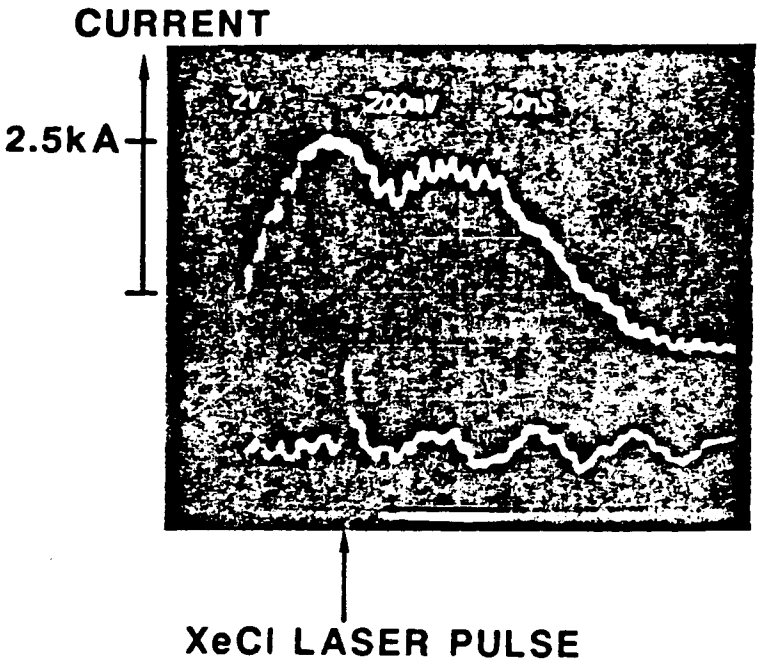

Fig. 3. Atypical current shape of XeCl laser discharge and the laser pulse shape.

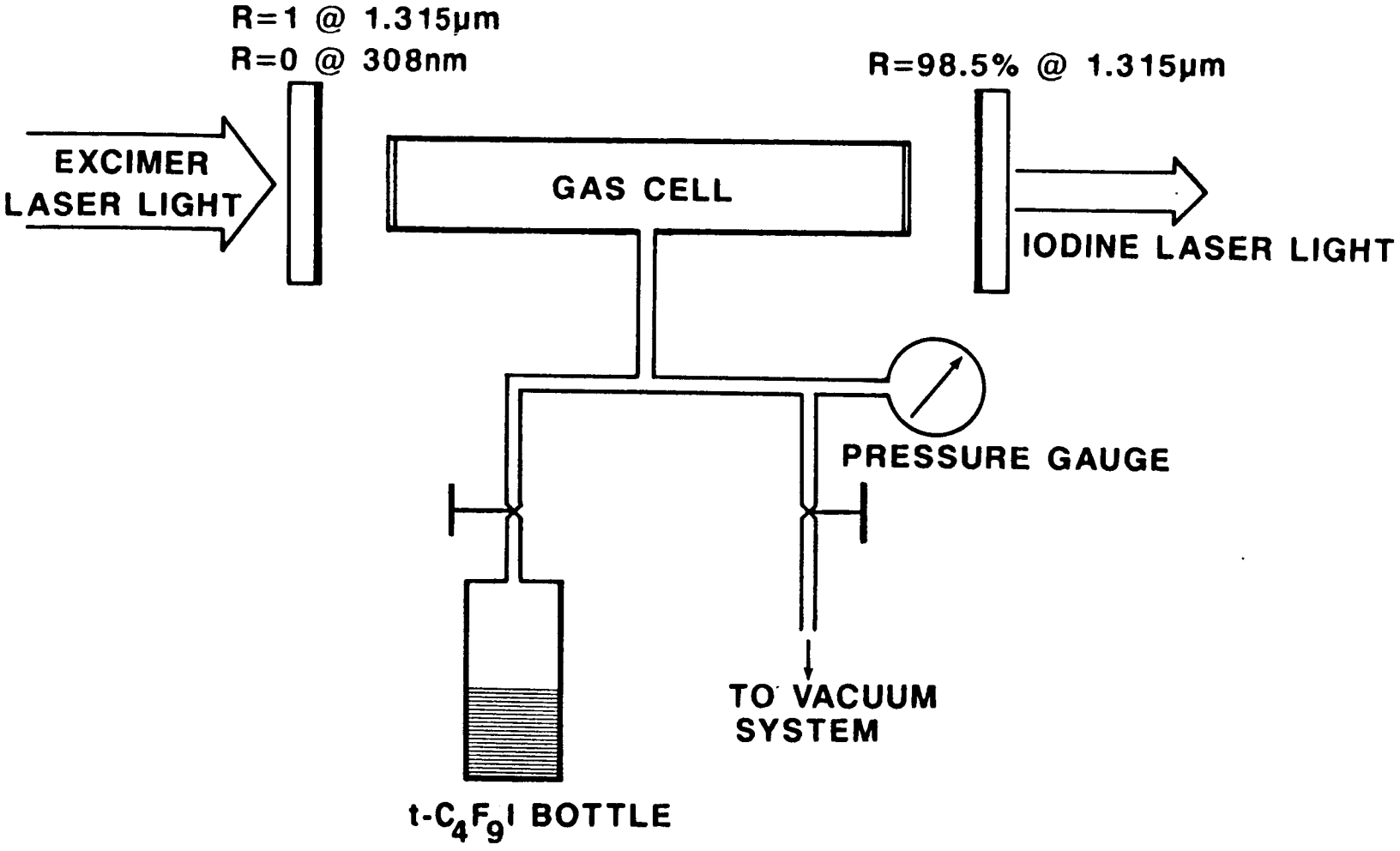

Fig. 4. Schematic diagram iodine laser oscillator.

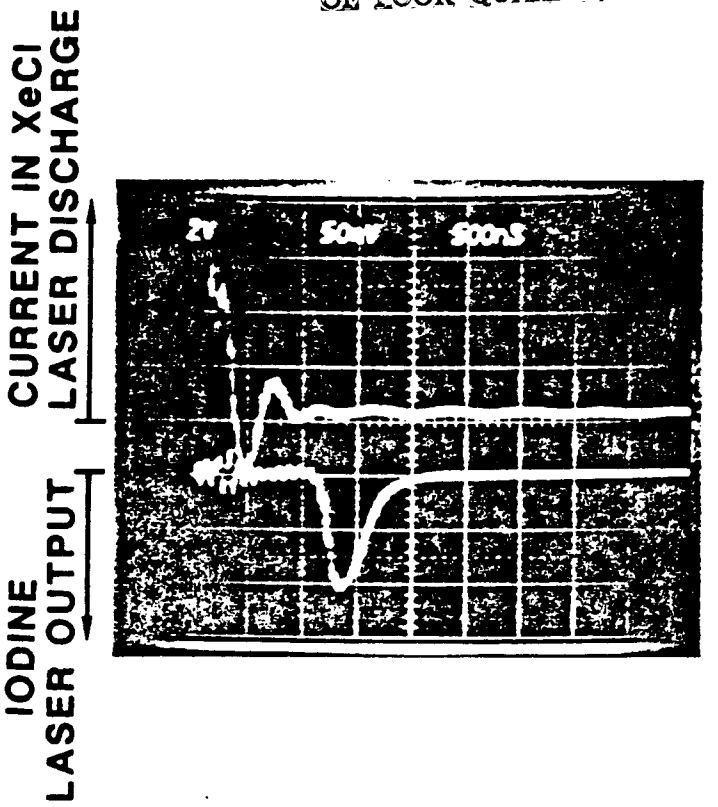

Fig. 5. Temporal characteristics of iodine laser output. The iodine laser output is delayed about 1 usec from the XeCl laser pulse.

II. KINETIC MODELING OF A SOLAR-PUMPED IODINE LASER

by Larry V. Stock

Kinetic Modeling of a Solar-Pumped Iodine Laser

An algorithm of the kinetic model is developed which predicts the output power of a solar-pumped iodine laser more precisely. Previous reports[1,2] showed good agreement between the theoretical model and experimental data given as a function of fill pressure of a flashlamp-pumped iodine laser oscillator system with an elliptical pumping cavity and pumping times of about one millisecond. Using the kinetic reaction rate coefficients found before[1,2] for the lasants i-C_3F_7I, n-C_4F_9I, and t-C_4F_9I; the power output of the laser has been calculated as a function of time for different pumping intensities with a constant fill pressure. Again, there is good agreement between theoretical predictions and experimental data. In addition to the new data sets being examined, a calculation method of the set of differential equations is used which is an order of magnitude faster that the previous calculation. This new method will speed the process of adjusting the reaction rate constants such that the theoretical model best represents the experimental data. Later, this model can be extrapolated to establish the scalability of a solar-pumped iodine laser system for space-to-space power transmission.

In order to ensure accuracy and improve the efficiency of the calculations, the initial density of the lasant is scaled to unity and the set of equations are solved by a forth-order Runge-Kutta method due to Fehlberg[3] with a variable step size. In scaling the species gas density, it is noted that the three-body reactions are scaled quadratically by the number density of the lasant, where the two-body reactions are scaled linearly. This can be interpreted as, the recombination of atomic iodine with a free radical is increased linearly with pressure, the formation of I_2 increases quadradically. This is demonstrated by the data; the lasing time decreases as the fill pressure increases (figs. 1, 2, and 3).

The speed of the calculation has been increased by using a variable step size Runge-Kutta method. This method is best suited to problems which are not stiff numerically, therefore, the quasi-steady state solution[4] is used for optimum speed. This solution assumes that as the system is initially pumped,

the output of the oscillator is negligible before lasing threshold; and then after the system begins to lase, the relationship

$$d[\Delta I]/dt = 0$$

is solved for the stimulated emission rate, where $[\Delta I]$ is the inversion density. This eliminates the differential of the photon density in the oscillator.[4] The calculation of the set of differential equations for this system is further enhanced by solving for the lasing threshold time using the relationship that, intially, the gain is directly proportional to the square of the pumping time t, or

$$[\Delta I] \propto t^2$$

where the inversion density is directly proportional to the gain. Therefore, large time steps can be used to step the Runge-Kutta algorithm to the beginning of the laser pulse, rather than testing the calculation for threshold conditions using a relatively small step size.

In establishing a scaling law for the laser system, it is necessary to construct a mathematical algorithm which can be applied to different iodine laser configurations. In figures 4, 5, and 6, theoretical predictions of the output parameters are given as a function of flashlamp intensities indicated by different capacitor bank voltages and found by using the reaction rate coefficients reported previously[2] (Tables I, II, and III). The reaction rate coefficients were found by fitting the experimental data given as a function of fill pressure for a constant flashlamp intensity (5 kV capacitor bank). The flashlamp intensity can be approximated by a linear function of the capacitor voltage which is used to energize the flashlamp. This relationship is reflected in the output energy of the laser as a function of capacitor voltage (figs. 4, 5, and 6). It should be noted that there is good agreement between the experimental data and theoretical predictions for the time-to-laser threshold and lasing time for the lasant n-C_4F_9I. Later, reaction rate coefficients will be found which incorporate both sets of data, and then these will be applied to another laser system [i.e., the long-gain length (one meter) iodine laser oscillator].

In figures 7, 8, and 9, the experimental data and the corresponding theoretical calculations for the output power is given for a fill pressure of 20 torr and a 5 kV capacitor bank. Figures 10, 11, and 12 show a quantitative value for the relative merit of the lasant for the same fill pressure and flashlamp intensity. The relative merit is defined as twice the molecular iodine density given as a function of flashlamp pulse time divided by the total number of photodissociations of the parent molecule. This value relates the loss of lasant material to the energy available in the oscillator. The lasant t-C_4F_9I (fig. 12) would be expected to have the smallest value of the three lasants considered, since it has the largest output energy; it does have the smaller value.

In addition, in figures 10, 11, and 12, a representation of the inversion density is shown.[4] In the key the number density (molec./cm^3) is given at one millisecond $[I_2]_f$ and as time approaches infinity $[I_2]_\infty$. In these figures, the gain is directly proportional to the square of the pumping time before threshold. Then after threshold, for the quasi-steady-state solution,[4] the inversion density is a constant value; until, basically, $[I_2]$ becomes sufficient to quench the laser.

To improve a kinetic model for a solar-pumped iodine laser, the following steps summarize the accomplishments during this reporting period:

1. A new data set has been analyzed which is a function of pumping intensity for a specific fill pressure.

2. The computer algorithm used to solve the set of differential equations has been improved.

3. A new parameter has been defined which gives a quantitative value for the relative merit of the lasants as power sources.

REFERENCES

1. Larry V. Stock: "Kinetic Modeling of the Solar-Pumped Iodine Lasers," Semiannual Progress Report NASA Grant NAG-1-441, February 28, 1987.

2. L. V. Stock and J. W. Wilson: "A Kinetic Model for a Solar-Pumped Iodine Laser," International Laser Science Conference, November, 1987.

3. John H. Heinbockel: "A Theoretical Study of Photovoltaic Converters," Final Report Research Grant NAG-1-148, May 16, 1987.

4. L. V. Stock, J. W. Wilson, and R. DeYoung: "A Model for the Kinetics of a Solar-Pumped Long Path Laser Experiment," NASA TM 87668, May 1986.

TABLE I. – Reaction rate coefficients and their associated reactions for the lasant i-C_3F_7I along with the parameters used to modify the optical time constant (ref. 2).

Lasant Reactions	i-C_3F_7I Symbol	Reaction Rate Coefficient $(cm^3)^n/sec$
$R + I^* \rightarrow RI$	K_1	$.1633 \times 10^{-11}$
$R + I \rightarrow RI$	K_2	$.1336 \times 10^{-10}$
$R + R \rightarrow R_2$	K_3	$.4385 \times 10^{-11}$
$R + RI \rightarrow R_2 + I$	K_4	$.7663 \times 10^{-16}$
$R + I_2 \rightarrow RI + I$	K_5	$.1783 \times 10^{-11}$
$I^* + I + RI \rightarrow I_2 + RI$	C_1	$.1095 \times 10^{-32}$
$I + I + RI \rightarrow I_2 + RI$	C_2	$.5970 \times 10^{-31}$
$I^* + I + I_2 \rightarrow I_2 + I_2$	C_3	$.8000 \times 10^{-31}$
$I + I + I_2 \rightarrow I_2 + I_2$	C_4	$.3933 \times 10^{-29}$
$I^* + RI \rightarrow I + RI$	Q_1	$.1122 \times 10^{-15}$
$I^* + I_2 \rightarrow I + I_2$	Q_2	$.3400 \times 10^{-10}$
	T_s	.9206
	α	.0313

TABLE II. - Reaction rate coefficients and their associated reactions for the lasant n-C_4F_9I along with the parameters used to modify the optical time constant (ref. 2).

Lasant Reactions	n-C_4F_9I Symbol	Reaction Rate Coefficient $(cm^3)^n/sec$
$R + I^* \rightarrow RI$	K_1	$.7499 \times 10^{-12}$
$R + I \rightarrow RI$	K_2	$.9884 \times 10^{-11}$
$R + R \rightarrow R_2$	K_3	$.6065 \times 10^{-11}$
$R + RI \rightarrow R_2 + I$	K_4	$.7762 \times 10^{-16}$
$R + I_2 \rightarrow RI + I$	K_5	$.2240 \times 10^{-10}$
$I^* + I + RI \rightarrow I_2 + RI$	C_1	$.8688 \times 10^{-33}$
$I + I + RI \rightarrow I_2 + RI$	C_2	$.2182 \times 10^{-31}$
$I^* + I + I_2 \rightarrow I_2 + I_2$	C_3	$.8000 \times 10^{-31}$
$I + I + I_2 \rightarrow I_2 + I_2$	C_4	$.3933 \times 10^{-29}$
$I^* + RI \rightarrow I + RI$	Q_1	$.6412 \times 10^{-15}$
$I^* + I_2 \rightarrow I + I_2$	Q_2	$.3400 \times 10^{-10}$
	T_3	.9193
	α	.0262

TABLE III. - Reaction rate coefficients and their associated reactions for the lasant t-C_4F_9I along with the parameters used to modify the optical time constant (ref. 2).

Lasant Reactions	t-C_4F_9I Symbol	Reaction Rate Coefficient $(cm^3)^n/sec$
$R + I^* \rightarrow RI$	K_1	$.9328 \times 10^{-12}$
$R + I \rightarrow RI$	K_2	$.7051 \times 10^{-11}$
$R + R \rightarrow R_2$	K_3	$.2229 \times 10^{-13}$
$R + RI \rightarrow R_2 + I$	K_4	$.4755 \times 10^{-16}$
$R + I_2 \rightarrow RI + I$	K_5	$.1117 \times 10^{-11}$
$I^* + I + RI \rightarrow I_2 + RI$	C_1	$.3638 \times 10^{-32}$
$I + I + RI \rightarrow I_2 + RI$	C_2	$.4206 \times 10^{-31}$
$I^* + I + I_2 \rightarrow I_2 + I_2$	C_3	$.8000 \times 10^{-31}$
$I + I + I_2 \rightarrow I_2 + I_2$	C_4	$.3933 \times 10^{-29}$
$I^* + RI \rightarrow I + RI$	Q_1	$.9236 \times 10^{-15}$
$I^* + I_2 \rightarrow I + I_2$	Q_2	$.3400 \times 10^{-10}$
	T_s	.9300
	α	.0038

Figures

Figures 1, 2, and 3. - Theoretical predictions compared to experimental results for the output parameters of a flashlamp pumped laser oscillator for different fill pressures and a constant flashlamp fluence (5 kV).

Figures 4, 5, and 6. - Theoretical predictions compared to experimental results for the output parameters of a flashlamp pumped laser oscillator for different flashlamp fluences shown as capacitor energy and a constant fill pressure (20 torr).

Figures 7, 8, and 9. - Theoretical calculation of the output power of the laser using the quasi-steady state model compared to the experimental data for different fill pressures and flashlamp intensities. The flashlamp pulse shape is given as a reference.

Figures 10, 11, and 12. - Theoretical predictions of the inversion density [ΔI] and subsequent gain normalized to one at threshold, and the representation of the relative merit of the lasant is shown, as discussed in the text. The flashlamp pulse shape is given as a reference.

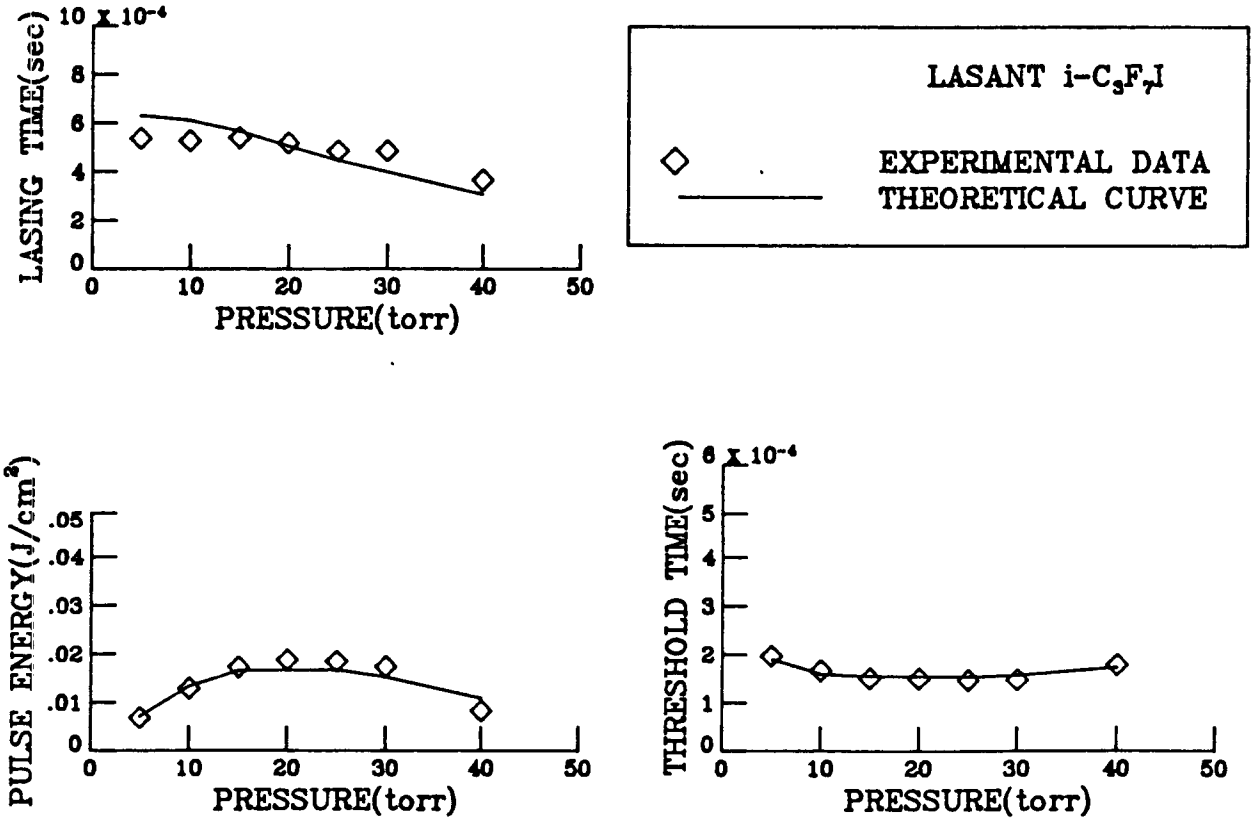
LASING TIME(sec)
10 X 10⁻⁴
8
6
4
2
0
0
10
20
30
40
50
PRESSURE(torr)
LASANT i-C3F7I
EXPERIMENTAL DATA
THEORETICAL CURVE
PULSE ENERGY(J/cm²)
.05
.04
.03
.02
.01
0
0
10
20
30
40
50
PRESSURE(torr)
THRESHOLD TIME(sec)
6 X 10⁻⁴
5
4
3
2
1
0
0
10
20
30
40
50
PRESSURE(torr)

FIGURE 1.

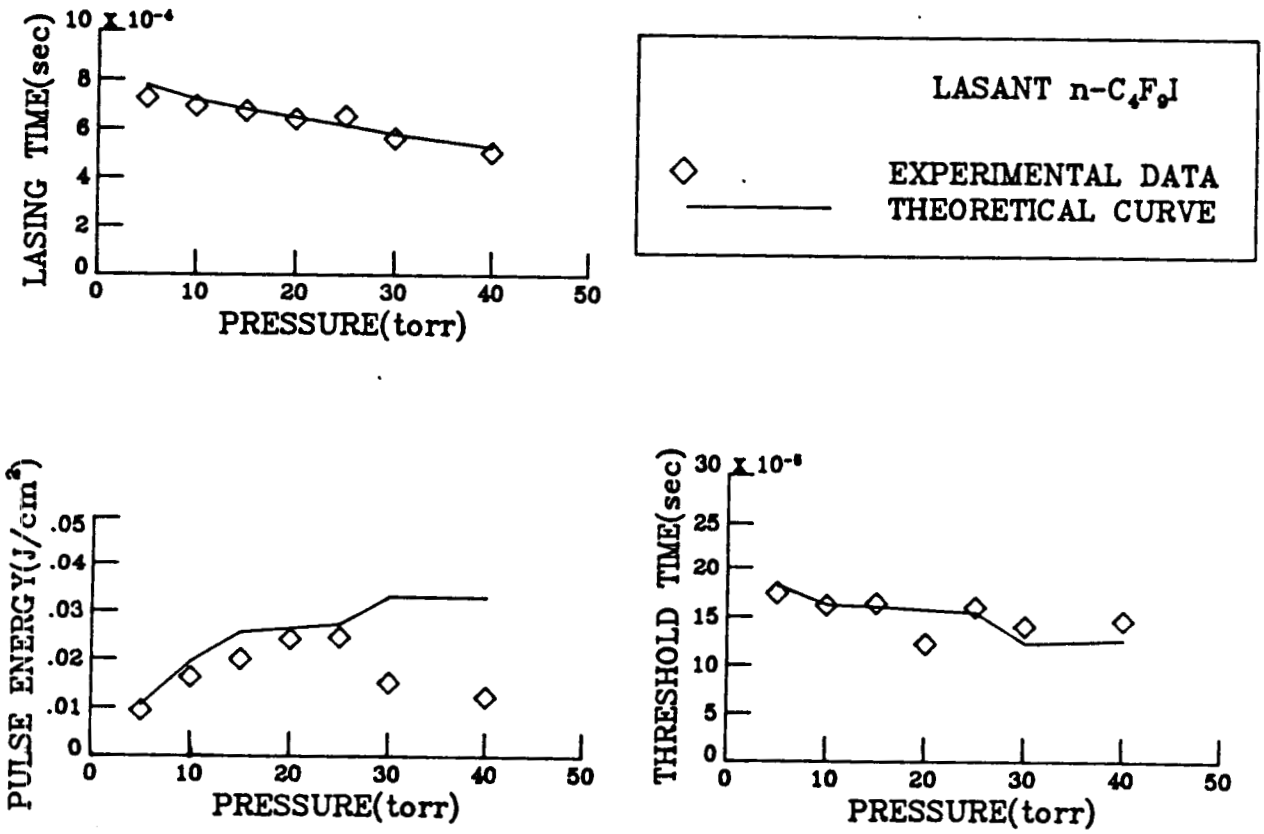
LASING TIME(sec)
10 X 10⁻⁶
8
6
4
2
0
0
10
20
30
40
50
PRESSURE(torr)
LASANT n-C₄F₉I
EXPERIMENTAL DATA
THEORETICAL CURVE
PULSE ENERGY(J/cm²)
.05
.04
.03
.02
.01
0
0
10
20
30
40
50
PRESSURE(torr)
THRESHOLD TIME(sec)
30 X 10⁻⁶
25
20
15
10
5
0
0
10
20
30
40
50
PRESSURE(torr)

FIGURE 2.

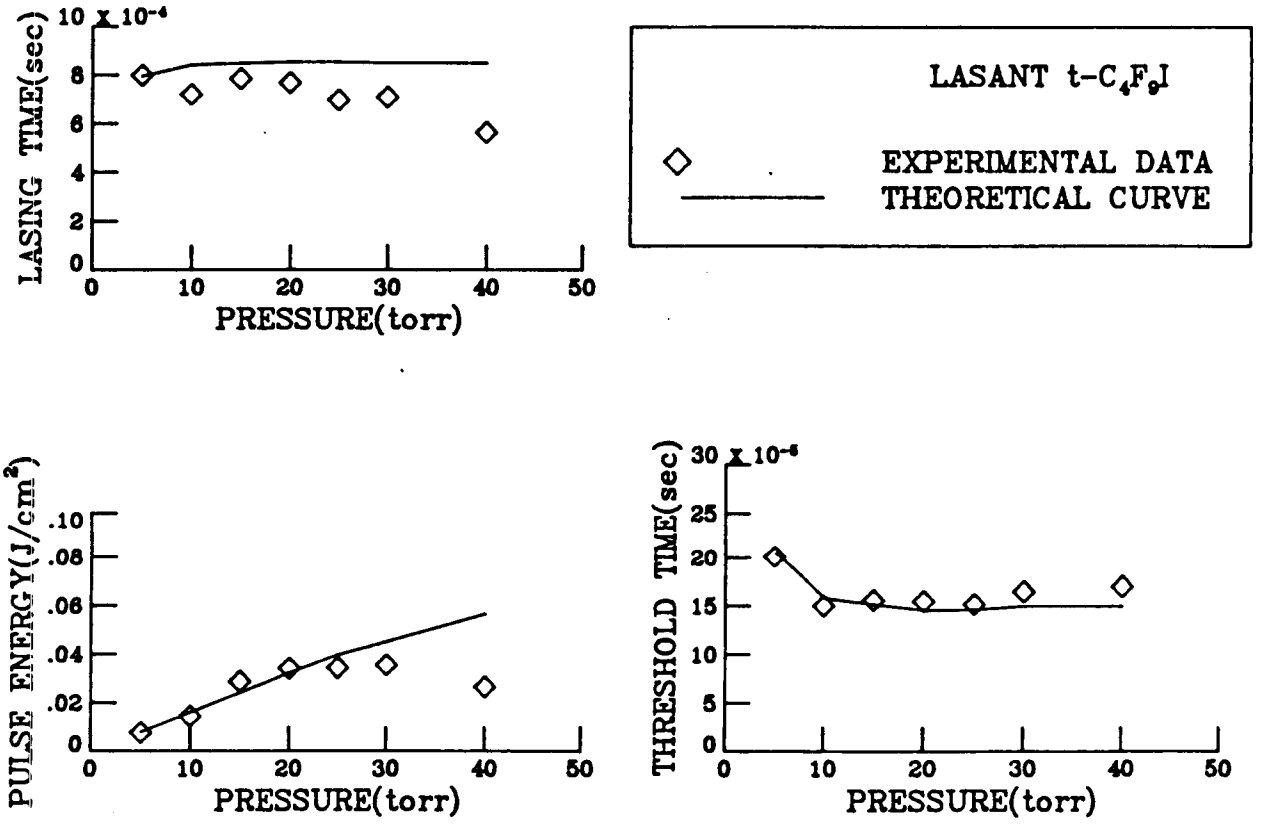
LASING TIME(sec)
10 X 10⁻⁴
8
6
4
2
0
0
10
20
30
40
50
PRESSURE(torr)
LASANT t-C₄F₉I
EXPERIMENTAL DATA
THEORETICAL CURVE
PULSE ENERGY(J/cm²)
.10
.08
.06
.04
.02
0
PRESSURE(torr)
THRESHOLD TIME(sec)
30 X 10⁻⁶
25
20
15
10
5
0
PRESSURE(torr)

FIGURE 3.

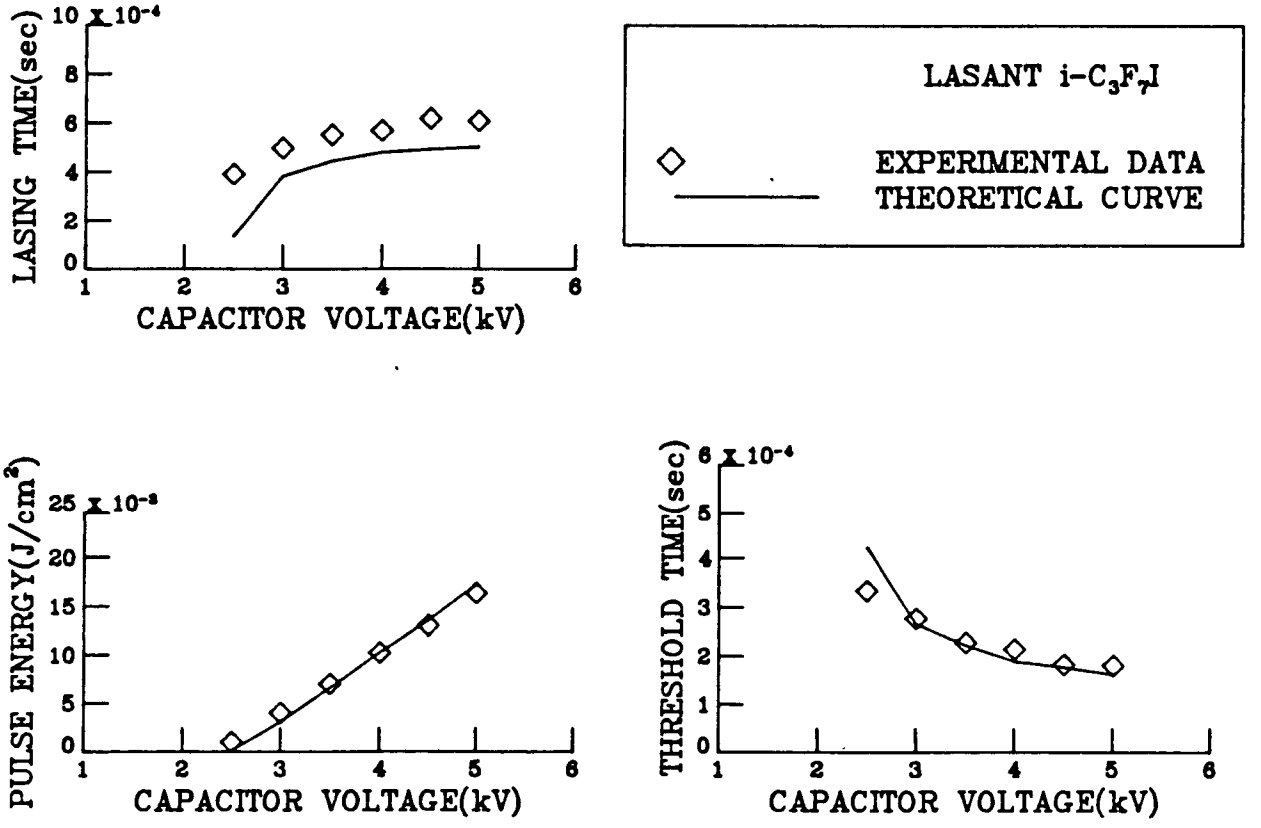
LASING TIME(sec)
10 X 10⁻⁴
8
6
4
2
0
1
2
3
4
5
6
CAPACITOR VOLTAGE(kV)
LASANT i-C3F7I
EXPERIMENTAL DATA
THEORETICAL CURVE
PULSE ENERGY(J/cm²)
25 X 10⁻³
20
15
10
5
0
1
2
3
4
5
6
CAPACITOR VOLTAGE(kV)
THRESHOLD TIME(sec)
6 X 10⁻⁴
5
4
3
2
1
0
1
2
3
4
5
6
CAPACITOR VOLTAGE(kV)

FIGURE 4.

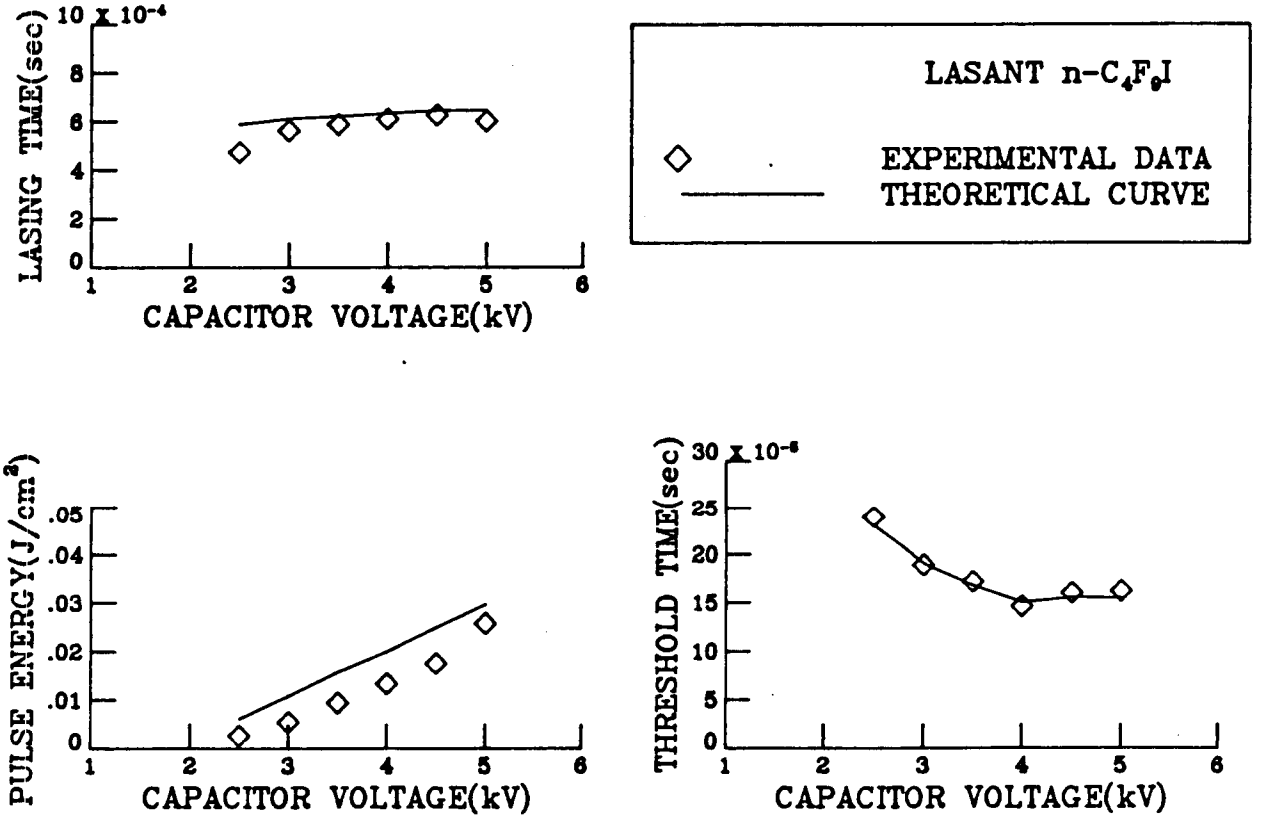
LASING TIME(sec)
10 X 10⁻⁴
8
6
4
2
0
1
2
3
4
5
6
CAPACITOR VOLTAGE(kV)
LASANT n-C₄F₉I
EXPERIMENTAL DATA
THEORETICAL CURVE
PULSE ENERGY(J/cm²)
.05
.04
.03
.02
.01
0
CAPACITOR VOLTAGE(kV)
THRESHOLD TIME(sec)
30 X 10⁻⁶
25
20
15
10
5
0
CAPACITOR VOLTAGE(kV)

FIGURE 5.

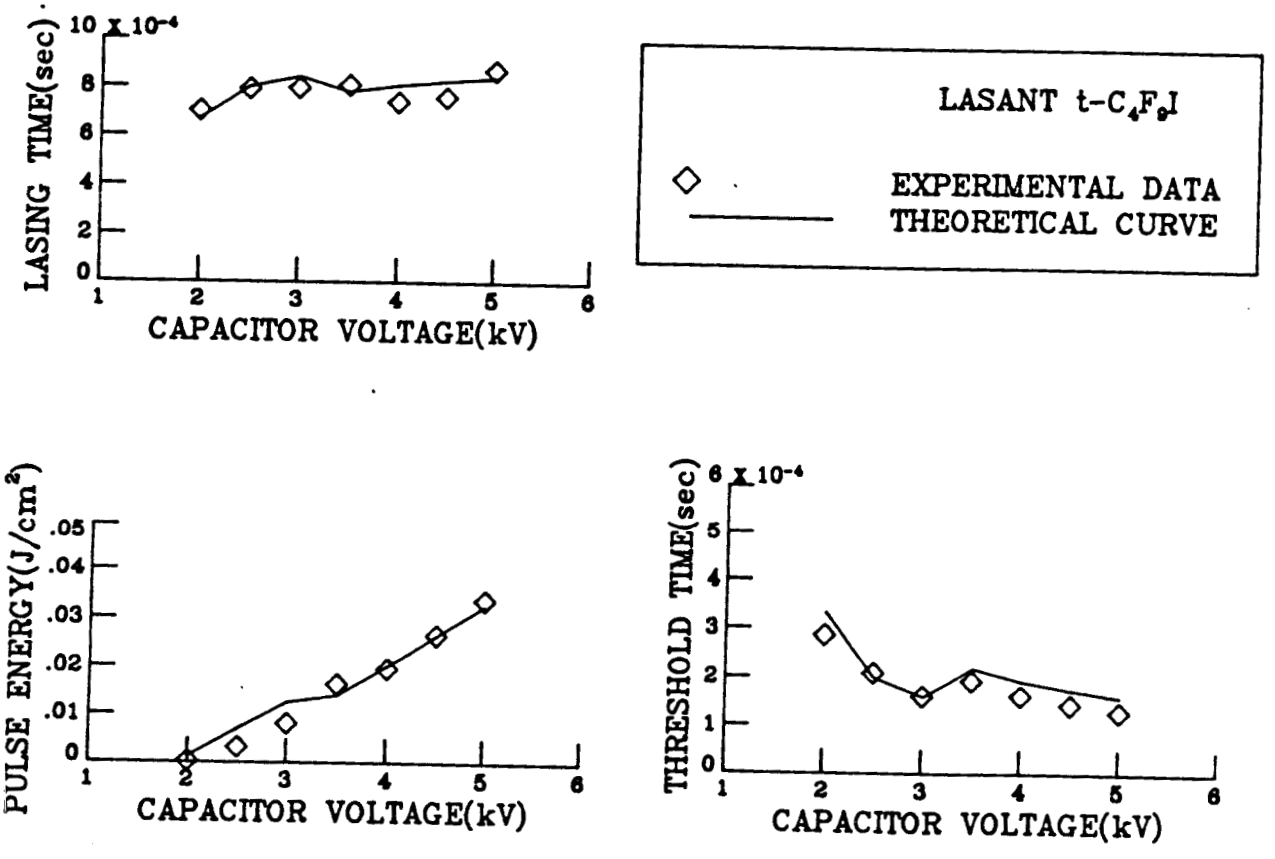
LASING TIME(sec)
10 X 10⁻⁴
8
6
4
2
0
1
2
3
4
5
6
CAPACITOR VOLTAGE(kV)
LASANT t-C₄F₉I
EXPERIMENTAL DATA
THEORETICAL CURVE
PULSE ENERGY(J/cm²)
.05
.04
.03
.02
.01
0
CAPACITOR VOLTAGE(kV)
THRESHOLD TIME(sec)
6 X 10⁻⁴
5
4
3
2
1
0
CAPACITOR VOLTAGE(kV)

FIGURE 6.

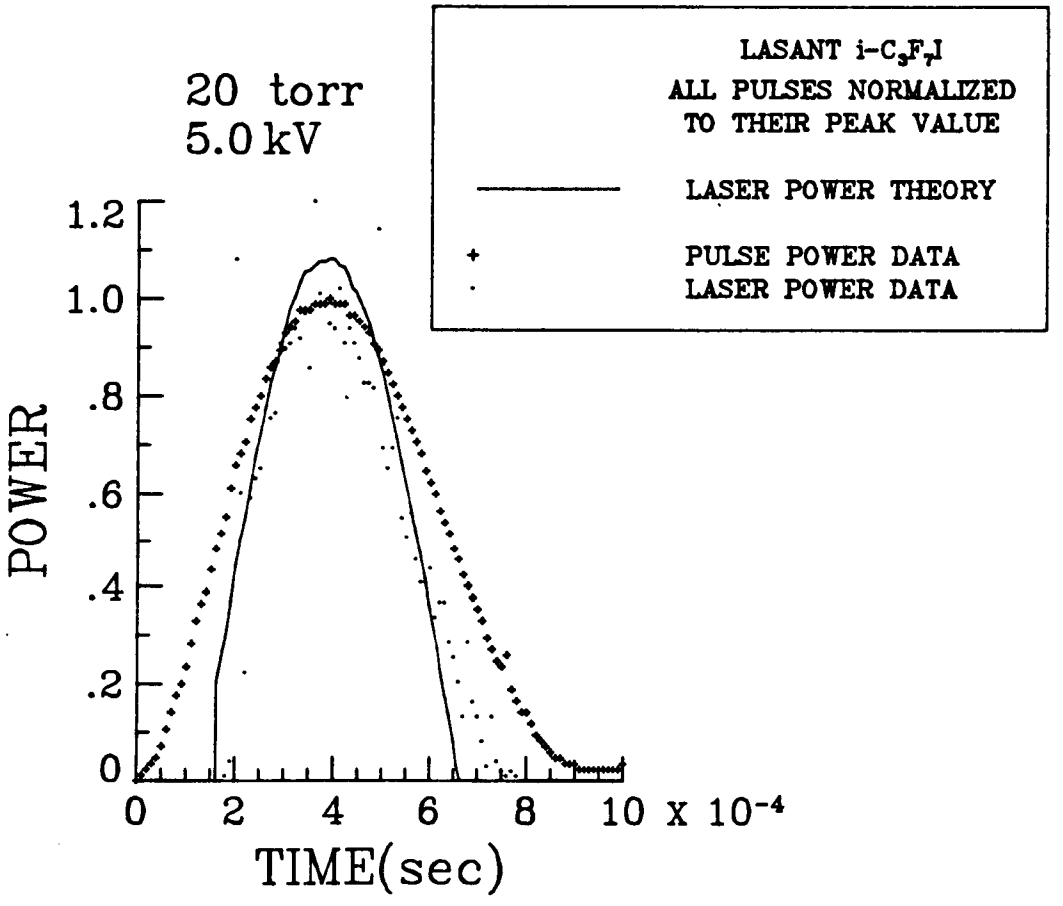
LASANT i-C3F7I
ALL PULSES NORMALIZED
TO THEIR PEAK VALUE
LASER POWER THEORY
PULSE POWER DATA
LASER POWER DATA
20 torr
5.0 kV
POWER
1.2
1.0
.8
.6
.4
.2
0
0
2
4
6
8
10 x 10-4
TIME(sec)

FIGURE 7.

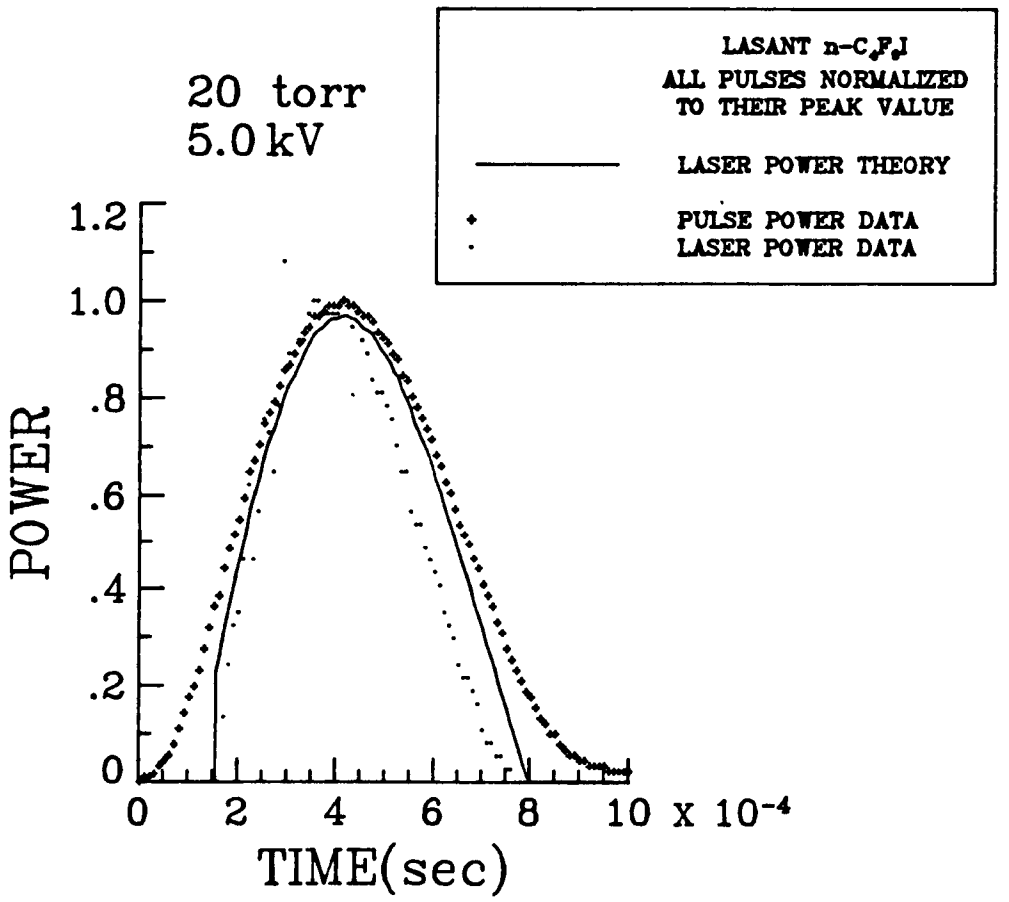
LASANT n-C4F9I
ALL PULSES NORMALIZED
TO THEIR PEAK VALUE
LASER POWER THEORY
PULSE POWER DATA
LASER POWER DATA
20 torr
5.0 kV
POWER
1.2
1.0
.8
.6
.4
.2
0
0
2
4
6
8
10 X 10-4
TIME(sec)

FIGURE 8.

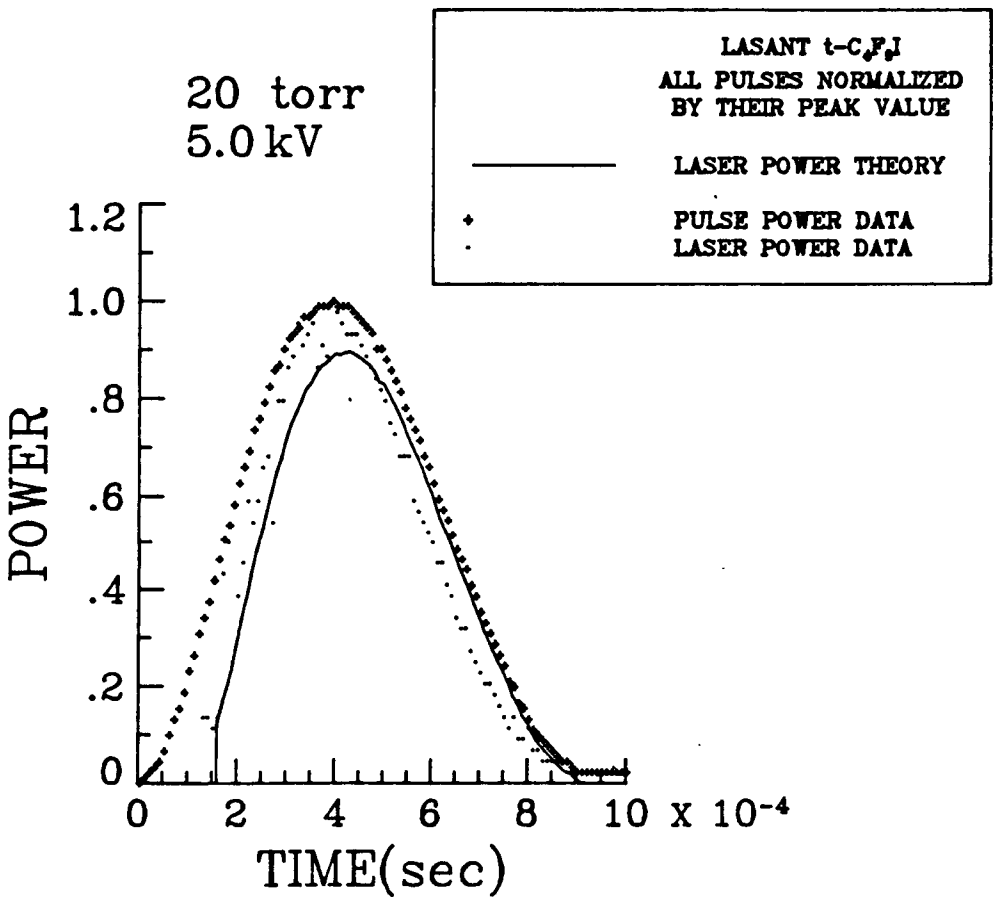
LASANT t-C4F8I
ALL PULSES NORMALIZED
BY THEIR PEAK VALUE
LASER POWER THEORY
PULSE POWER DATA
LASER POWER DATA
20 torr
5.0 kV
POWER
1.2
1.0
.8
.6
.4
.2
0
0
2
4
6
8
10 X 10-4
TIME(sec)

FIGURE 9.

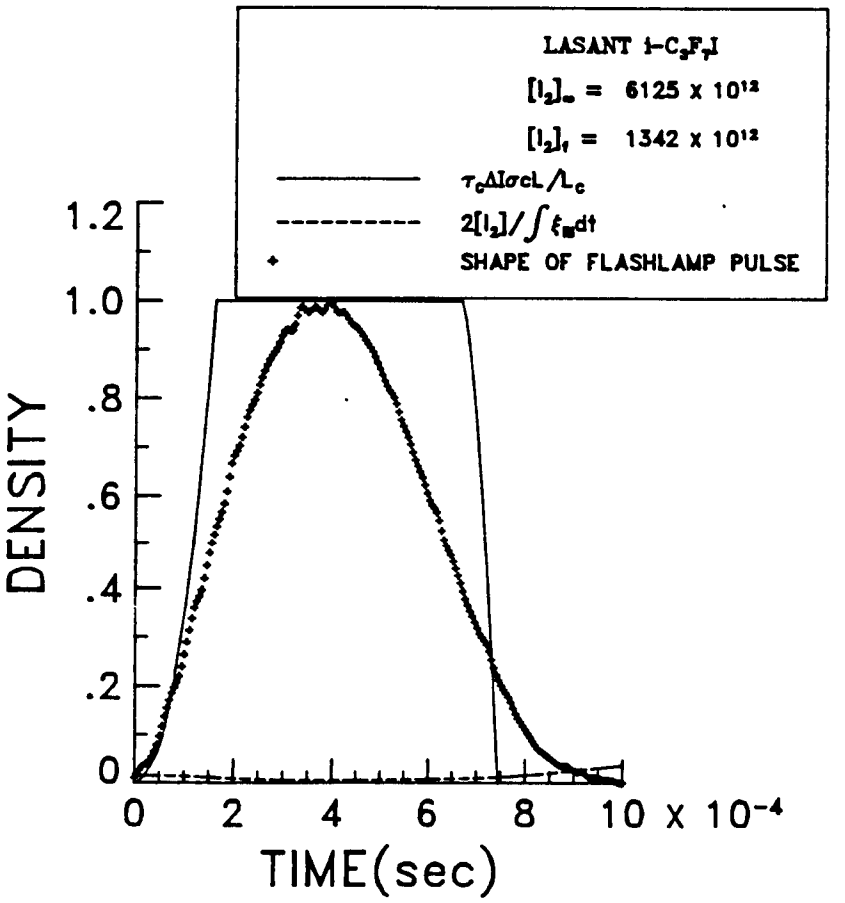
LASANT i-C3F7I
[I2]∞ = 6125 x 10^12
[I2]t = 1342 x 10^12
τcΔIσcL/Lc
2[I2]/∫ξmdt
SHAPE OF FLASHLAMP PULSE
DENSITY
1.2
1.0
.8
.6
.4
.2
0
0
2
4
6
8
10 x 10^-4
TIME(sec)

FIGURE 10.

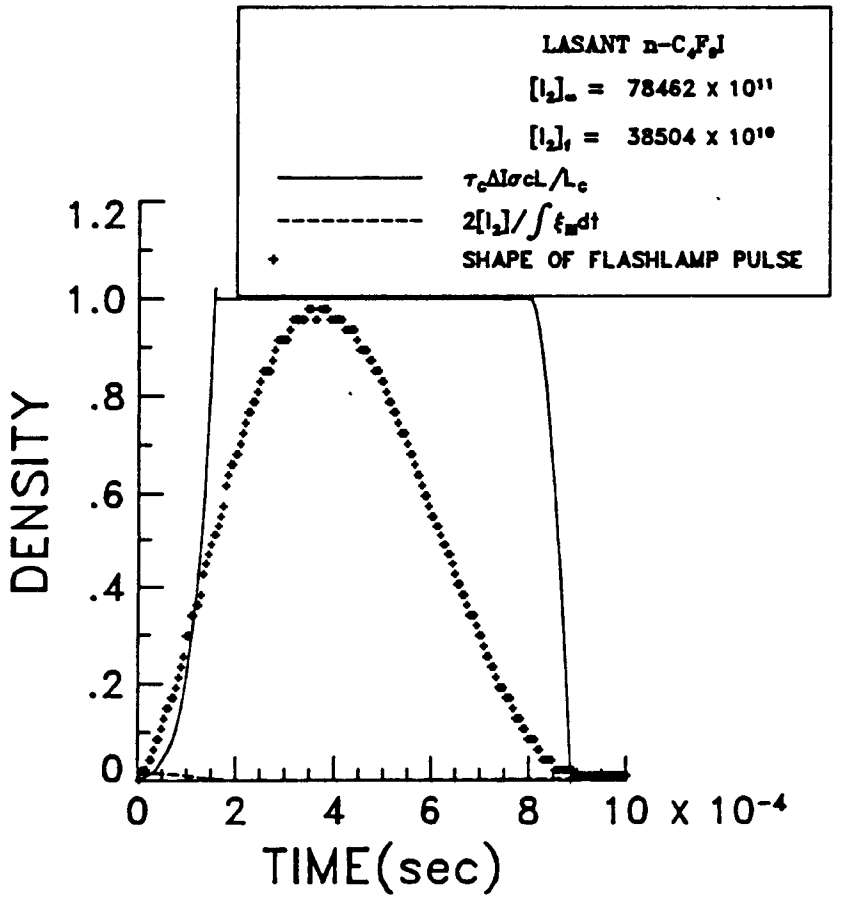
LASANT n-C4F9I
[I2]o = 78462 x 10^11
[I2]f = 38504 x 10^10
τcΔIσcL/Lc
2[I2]/∫ξmdt
SHAPE OF FLASHLAMP PULSE
DENSITY
1.2
1.0
.8
.6
.4
.2
0
0
2
4
6
8
10 x 10^-4
TIME(sec)

FIGURE 11.

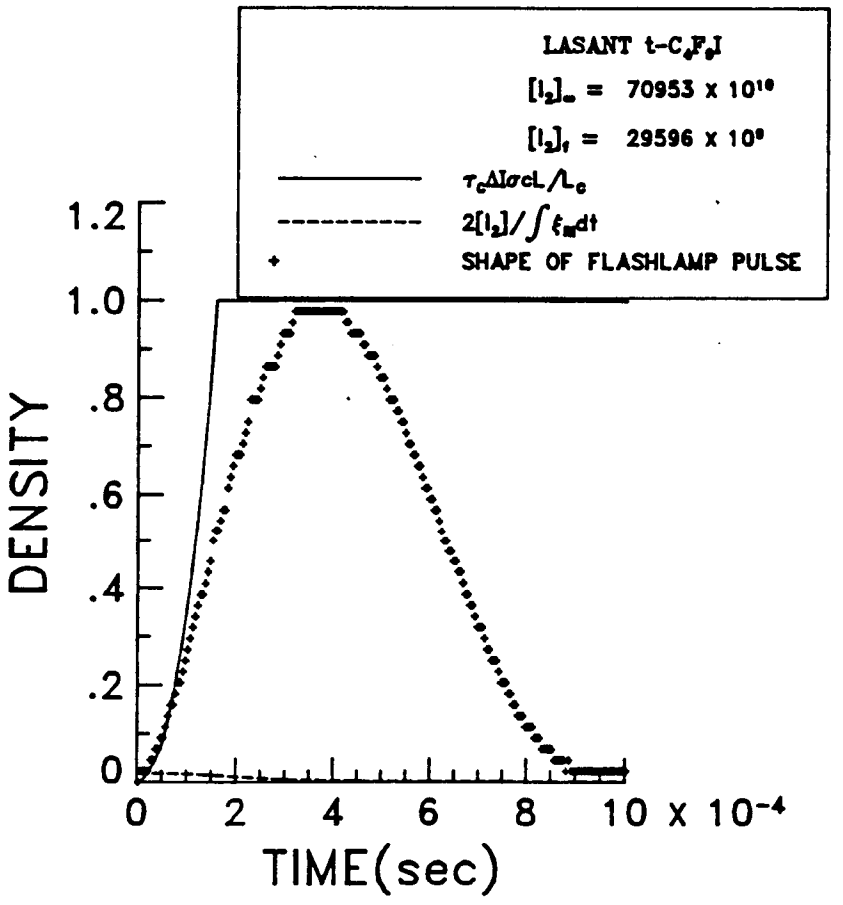
LASANT t-C4F9I
[I2]∞ = 70953 x 10^16
[I2]t = 29596 x 10^9
τcΔIσcL/Lc
2[I2]/∫ξMdt
SHAPE OF FLASHLAMP PULSE
DENSITY
1.2
1.0
.8
.6
.4
.2
0
0
2
4
6
8
10 x 10^-4
TIME(sec)

FIGURE 12.

III. EVALUATION OF SOLID STATE LASER MATERIALS FOR SOLAR-PUMPING

by Kyong H. Kim

A. Introduction:

A study on the evaluation of various solid state laser materials for solar-pumping has been performed during the period from January 1, 1987 to February 29, 1988 under NASA grant NAG-1-441 and this report provides the final summary. The literature survey on material characteristics and lasing efficiencies of a number of solid state laser materials such as Ruby, Nd:YAG, Nd:Glass, Cr:Nd:GSGG, Nd:YLF, Alexandrite and Emerald, has been reported in the previous semiannual progress report [Ref. 1]. In addition, theoretical calculations for solar-beam absorption by each crystal at various dopant concentrations and rod diameters, and for temperature distribution within laser crystal rods with various cooling water flow rates, have been also provided in the report. Even though there are many kinds of solid state laser materials available at the present time, only a few of them are appropriate for the candidate material for the solar-pumped high power laser application which requires the following material characteristics: (1) efficient pumping (i.e., absorption) bands near the peak of the solar spectrum, (2) long fluorescence lifetime, (3) good quantum efficiency, (4) good thermal conductivity, (5) high thermal resistance and (6) mechanical strength. Three crystals which are Nd:YAG, Cr:Nd:GSGG and Nd:YLF were appropriate for those requirements and experimentally studied in this research.

The Nd:YAG crystal has been well developed for many other applications in commercial markets, and the achievement of a 100 W CW laser power from the crystal with the solar-pumping is well known [Ref. 2]. However, the Nd:YAG crystal is very inefficient in the utilization of solar radiation as a pump source because of its very narrow absorption bands. Recently it was expected by us and by others that the new material, Cr:Nd:GSGG, would utilize the solar beam effectively and do better laser performance. Unfortunately, it was observed in our experiment that both the large amount of solar beam absorption by the broad absorption bands of the Cr^{3+}-ions in the Cr:Nd:GSGG crystal and the relatively poor thermal conductivity of the host material compared to that of Nd:YAG caused a large radial temperature variation in the Cr:GSGG rod and made the CW laser operation impossible at the pump power densities above 1,500 solar constants (203 w/cm^2). The difficulty of the CW laser

operation of the Cr:Nd:GSG crystal was also discussed in a recent paper by N. P. Barnes, et al., [Ref. 3]. On the other hand, the Nd:YLF crystal has been known as a material with a long upper state lifetime, a low threshold pump power requirement, smaller thermal lensing effect and higher efficiency on TEM_{00} single mode laser operation compared to other materials [Refs. 4-11]. This Nd:YLF crystal has been recognized to be a good CW laser material with a solar-simulator pumping in our experiment. It was also observed that the Nd:YLF crystal has greater thermal lensing effect than Nd:YAG in CW laser operation. This is opposed to the results observed by J. E. Murray [Ref. 10] in their pulsed operation in which the Nd:YLF showed lower thermal lensing than Nd:YAG. The experimental methods, results, theoretical analysis and conclusion will be presented in the following sections.

B. Experimental Methods and Results

The experiment performed in this research consists of (1) spectrum and power measurement of the pump beam and (2) laser performance measurement of the three crystals, Nd:YAG, Cr:Nd:GSGG and Nd:YLF. In order to determine the threshold pump power and slope efficiency of the crystals accurately, the spectral and spatial distributions of the Tarmarack solar-simulator beam intensity at the position of the crystal were carefully measured, and their absolute spectral intensities were obtained by calibration with a standard Tungsten lamp.

(1) Tarmarack Solar-Simulator Beam Measurement: A Tarmarack solar-simulator which consists of a Xe-arc lamp and an elliptical reflector was used as a pumping source and its beam was focused by a conical aluminum collector along the cone axis as shown in Fig. 1. The solar-simulator's beam intensity at the cone axis and its spectral shape were measured and reported in the previous semiannual progress report [Ref. 1]. The measured maximum solar-simulator's beam intensity at the peak point on the cone axis was 1,000 solar constants (135 w/cm^2) at the solar-simulator's input current of 200 A which was the lowest operating current. Since the threshold pump power densities of the three crystals were expected to be lower than 1,000 solar constants, a few numbers of diffused glass tubes

were placed at the cone axis as indicated by the dotted lines in Fig. 1 to lower the threshold pump power density. A 1/4" aluminum tubing with a small hole on its surface was placed at the cone axis. The hole allowed the solar-simulator beam to enter into the tubing and to be reflected at a 45° diffused surface which was made of a teflon bar and located inside the tubing. Then, the reflected beam was sent to the OMA detector through the fiber optics and spectrograph. The optical multichannel analyzer (OMA) and its detector used were Tracor Northern Model TN-6500 and TN-6132, respectively. The spectrograph used in this measurement was Jarrell-Ash Model 82-498 (MonoSpec 27) and one of its three gratings which has 150 grooves/mm with blaze angle at 0.4 μm was used. The absolute intensity of the solar-simulator's beam was calibrated with a 45-W standard tungsten lamp (Optronics lab. Model 345 RP) by placing the aluminum tubing connected to fiber optics and diffuser in front of it. Figure 2 shows the distribution of the solar simulator's beam intensities at a 1/8" rod surface along the cone axis inside various glass tubes for the solar-simulator's input current of 200 A. The peak intensity with a transparent glass tube was about 930 solar constants (126 w/cm^2) and that with three diffused glass tubes was about 200 solar constants (27 w/cm^2). With the three diffused glass tubes, the pump beam was more uniformly distributed along the cone axis. Figure 3 shows the peak intensity variation at various solar-simulator input currents. The maximum pump beam intensity achieved with our system was about 3,100 solar constants (419 W/cm^2).

(2) Solar-Simulator Pumped Laser Experiment: Figure 4 shows the experimental setup used for CW and quasi-CW laser operation of the three crystals with the Tamarack solar-simulator as a pumping source. Each crystal had a size of 1/8" diameter and 3" length, and had highly-reflective (HR) mirrors with a curvature of 5 m radius coated directly at one end and anti-reflection coatings at the other end. The previous experimental setup which was discussed in Ref. 1 had a separate HR mirror which was located near the center collector cone. With that geometry it was very difficult to have a CW laser operation because the HR mirror was moved out of alignment by the thermal effect caused by the pump light. With the highly reflective mirror directly coated on one end of the

crystals, CW laser operation was successfuly achieved for the Nd:YAG and Nd:YLF crystals up to the pump power density of 2,000 solar constants.

On the other hand, the CW laser operation was possible only up to 1,500 solar constants for the Cr:Nd:GSGG crystal. For the pump beam intensities above 1,500 solar constants the lasing appeared instantly after the pump beam illumination, and disappeared immediately. The lasing lasted for less than one second. However, when a chopper was used to pulse the pump beam, continuously pulsed lasing was achieved at various chopper speeds from 0.6 Hz to 13 Hz. The ratio of chopper's open-to close section was one, and the opening was 0.35 s duration at 0.7 Hz. The lasing lasted as long as the chopped pump period. This stable quasi-CW laser operation was possible at pump power densities below 2,500 solar constants (=338 W/cm^2) at which the peak laser output power was about 340 mW and the corresponding average power was 170 mW. However, for the pump power density of 3,000 solar constants (=405 W/cm^2) even the quasi-CW lasing started to be unstable and disappeared 1.5 seconds after initial lasing. This GSGG crystal started cracking within the rod by thermal loading when the quasi-CW laser operation was performed at a high pump power density of about 3,000 solar constants (=405 w/cm^2) for several minutes. The laser cavity stability condition affected by the thermal lensing effect on the crystal will be calculated and compared with the experimental result in the following chapter.

Figures 5 through 8 show the absorption spectra of the three different crystals with the particular doping concentrations used in our experiment. The Nd:YAG crystal used here had 1.1 atomic percent doping concentration and its absorption coefficient was calculated from the data given in Refs. 12 and 13. The Cr:Nd:GSGG crystal used had doping densities of 2×10^{20} $ions/cm^3$ for each of Cr^{3+}- and Nd^{3+}- ions, and its absorption coefficient was obtained from the absorption spectrum of the same kind of material measured by J. A. Williams [Ref. 14]. The Nd:YLF crystal used here had about 1.5 atomic percent doping density for the Nd^{3+}- ion and its absorption coefficient was calculated from the data given in Ref. 4.

The solar beam absorption efficiencies of the crystals of the particular doping densities and 3.2 mm thickness are 5.7 percent for the

Nd:YAG, 32.1 percent for Cr:Nd:GSGG, 3.8 percent for π -polarization of Nd:YLF and 2.8 percent for σ -polarization of Nd:YLF.

Figure 9 shows the results of the Nd:YAG and Nd:YLF crystals under the solar-simulator pumping. The size of each crystal was 3.2 mm diameter by 3" length. The slope efficiencies, threshold pump powers and threshold absorbed pump power densities are listed in Table 1. The threshold absorbed pump power densities were calculated by

$$\text{Threshold absorbed pump power density} = \frac{(\text{Threshold pump power}) \times (\text{Absorption efficiency})}{(\text{Crystal volume})}$$

It is seen from the Table that the threshold of Nd:YLF is lower than that of Nd:YAG and the slope efficiency of Nd:YLF is also slightly higher than that of Nd:YAG. The low threshold pump power requirement of the Nd:YLF crystal can be attributed to its longer upper state lifetime and smaller refractive index values. The higher slope efficiency of the Nd:YLF than that of Nd:YAG at the low pump power densities may be explained by its smaller absorption coefficient compared to the YAG's which enables the pump power density over the entire crystal volume to be above the threshold. Since the absorption coefficient of Nd:YAG is generally more than two times greater than that of Nd:YLF, most pump beam is absorbed at the surface of the Nd:YAG rod for low pump power densities, and eventually it leaves the inner portion of the crystal at below the threshold. Thus, more ions in the Nd:YLF crystal involve in the lasing action than in Nd:YAG, and provide better slope efficiency. The reflectance of the optimum otuput coupling mirror was about 95 percent for both Nd:YAG and Nd:YLF crystals, which are shown in Figs. 9, 10, 11 and 17. Figures 10 and 11 were taken at pump power densities higher than those used in Fig. 9 for the Nd:YAG and Nd:YLF crystals, respectively. Figure 17 was taken by using a flashlamp as a pumping source and will be discussed in the next section. When flat output mirrors were used for the Nd:YLF crystal under the solar-simulator pumping, the lasing appeared instantly as soon as the solar-simulator's bean was illuminated, and lasted for less than one second. No continuous lasing was achieved with flat mirrors for the Nd:YLF crystal at both low and high pump power densities while it was successfully achieved for the Nd:YAG. This means that the thermal lensing

effect of the Nd:YLF crystal is greater than that of the Nd:YAG undr a CW pumping.

Figures 12 and 13 show the CW laser outputs of two different diameters of Nd:YLF rods, one with 1/8" diameter and the other with 1/4" diameter as a function of pump power. Figure 12 was taken at low pump powers which was obtained by replacing the water jacket glass tube in Fig. 4 with a glass tube shown with a diffused outer surface and with 16 mm OD and 14m ID, and by adding two more diffused glass tubes of large diameters around it. Meanwhile, Fig. 13 was taken with a transparent glass tube for the water jacket. In both cases, the slope efficiency of the 1/8" rod was about 0.13 percent. The slope efficiency of the 1/4" rod was increased from 0.16 percent at low pump powers to 0.26 percent at high pump powers. The measured threshold of the 1/8" Nd:YLF rod was about 167 W which corresponds to the pump power density of 275 solar constants and that of the 1/4" rod was about 195 W which corresponds to pump power density of 320 solar constants. The possible explanation of these results is that the large diameter of the crystal requires strong pump beam intensity to have its entire volume placed above the threshold condition and provides a high slope efficiency compared to the small diameter of the rod for strong pump beam intensities.

Figure 14 shows the laser outputs of 1/8" diameter Nd:YLF rod with water circulation and with circulation of a Coumarine-4 dye solution circulation in the cooling jacket. A transparent glass tube with a smaller diameter (13 mm OD and 11 mm ID) was used here for the cooling jacket. The 4 M concentration of Exciton Courmine-4 (7 hydroxy 4 methy coumarine) in ethanol solution was used. Our data shows no enhancement with the dye solution and contradicts the result observed by Bhawakan and Pandit (Ref. 15). In Ref. 15, they claimed that they achieved about 38 percent decrease in threshold and nearly 50 percent increase in slope efficiency with a xenon flashlamp-pumped Nd:Glass laser. Because of our limited time, no further careful measurement has been made in this energy conversion experiment. The further experiment on this subject has to be performed to make a reasonable conclusion.

Figure 15 shows the measured average laser output power of the quasi-CW Cr:Nd:GSGG laser along with the CW laser outputs from Nd:YAG and Nd:YLF. Any comparison between data of the different crystals may not

have to be made in the figure because there exists some uncertainty on the data. It was intended to keep the system in the same condition between the experiments for each crystal, but it was very likely to be changed because there had been some amount of time interval between them and the condition of the xenon arc lamp in the solar-simulator had become worse as time went on. In addition, the GSGG crystal was damaged by the thermal cracking after some measurements, and was not available when we had the other crystals. Another problem involved was that the highly-reflective mirror coating on the Nd:YAG crystal was also damaged after the measurement of one data set which is shown in Fig. 15. The HR mirror coating on the Nd:YAG crystal was just peeled off by different thermal expansions between YAG material and the coating itself during the high pump power operations. The Nd:YAG's data shown in the previous figures was taken after recoating a new HR mirror on the crystal. Contrary to the data shown in Fig. 15, the laser performance of Nd:YAG was almost the same as or slightly worse than with that of Nd:YLF in Fig. 5. Thus, the validity of the GSGG data as well as the Nd:YAG's data shown in Fig. 15 was left in question.

(3) Flashlamp Pumped Laser Experiment

Since the CW laser operation was difficult with the Nd:YLF crystal when flat output coupling mirrors were used and also with the Cr:Nd:GSGG crystal at high pump powers, a flashlamp lamp experiment was performed to have an idea on the laser performance of the two crystals with various output coupling mirrors which were available to us. The experimental setup used is shown in Fig. 16. The flashlamp and crystal rod were placed in an aluminum foil reflective cavity which was supported with a plexi-glass tube. The cavity length was about 16 cm long and the laser output was detected by a Melectron J3-05 energy meter and a Nicolet Model 204-A oscilloscope. The same Nd:YLF rod as the one used in the solar-simulator pumped experiment was used in the measurement of the data shown in Fig. 16. On the other hand, a broken piece of the Cr:Nd:GSGG rod from the previous experiment was prepared for the flashlamp experiment. The one end of the broken rod had the same original highly reflective mirror coating and the other broken end was optically polished. The entire length of this piece was 3.1 cm. The same experimental setup was used for

the GSGG except that both flashlamp and crystal were placed in a 11 mm OD and 14 mm ID glass tube, whose outer surface was wrapped with aluminum foil, to ensure a tight optical coupling instead of using the cavity used for the Nd:YLF. The cavity length for this GSGG was about 15 cm. Data shown in Fig. 18 was taken with this system. Then, a mylar sheet was placed between the flashlamp and the GSGG to lower the pump power densities on the crystal, and the data taken with this configuration was shown in Fig. 19.

From Figs. 5, 11, and 17 it can be concluded that the highest slope efficiency is achieved with a 95 percent reflectance mirror for the Nd:YLF. Figures 18 and 19 show that the slope efficiency and teh threshold of the Cr:Nd:GSGG increases as the output mirror reflectance decreases. Thus, the slope efficiency of the GSGG shown in Fig. 15 can be increased by having a low reflectance output mirror.

C. Theoretical Analysis on Thermal Focus of Cr:Nd:GSGG and Laser Cavity Stability.

The absorbed pump power by a crystal rod is written as

$$P_a = \int_{z=o}^{L} \int_{o}^{2\pi} \int_{\lambda 1}^{\lambda 2} I_o(\lambda,\phi,z) \left[1 - \exp\left\{-\epsilon(\lambda)\ell\right\}\right] d\lambda (1-\xi) r_o d\phi dz \qquad (1)$$

where $I_o(\lambda,\phi,z)$ is the spectral irradiance of the pumplight at the rod surface (W/cm^2), $\epsilon(\lambda)$ is the absorption coefficient of the crystal at a given wave-length λ (cm), ℓ is the pass length of the pump beam in the crystal (cm), ξ is the reflective loss coefficient of pump beam at rod surface, r_o is the rod radius (cm) and L is the length of rod (cm). The absorbed pump beam power by the crystal causes the radial temperature gradient which can be obtained by solving one-dimensional heat conduction equation (Ref. 16):

$$T(r) = T(r_o) + \frac{P_a}{4\pi r_o^2 KL}(r_o^2 - r^2) \qquad (2)$$

where K is the thermal conductivity of the crystal. Thus, the temperature difference between the rod surface and rod center is written as

$$T(o) - T(r_o) = \frac{P_a}{4\pi KL} \qquad (3)$$

this radial temperature gradient generates mechanical stresses in the laser rod and introduces the variation of the refractive index. The combined effect of a temperature- and a stress-dependent variation of the refractive index is expressed as (Ref. 16 and 17).

$$n(r) = n_o + \Delta n(r)$$

$$= n_o \left[1 - \frac{P_a}{2\pi r_o^2 K L} \left(\frac{1}{2n_o} \frac{dn}{dT} + n_o^2 \alpha C_{r,\phi}\right) r^2\right] \tag{4}$$

where n_o is the index of refraction of the crystal, α is the linear thermal expansion coefficient and C_r and C_ϕ are the elasto-optic constants for light with radial and tangential polarization. This radial variation of the refractive index makes the crystal behave like lens-like medium.

From the theoretical derivation shown in Appendix we obtain an equation for the focal length of the thermal lensing effect caused by the radial variation of the refractive index as

$$f = \left[\frac{2n_o}{b} \sin \frac{2L}{b}\right]^{-1} \tag{5}$$

and the G parameters for our laser resonator as

$$G_1 = \frac{a_1}{a_2}\left[\cos \frac{2L}{b} - \frac{2n_o d}{b} \sin \frac{2L}{b} - \frac{1}{R_1}\left(\frac{b}{2} \sin \frac{2L}{b} + n_o d \cos \frac{2L}{b}\right)\right] \tag{6}$$

$$G_2 = \frac{a_2}{a_1}\left[n_o \cos \frac{2L}{b} - \frac{1}{R_2}\left(\frac{b}{2} \sin \frac{2L}{b} + n_o d \cos \frac{2L}{b}\right)\right] \tag{7}$$

where d is the distance from the flat end of the rod to the output mirror and b is the measure of the degree of the variation of n which can be expressed as

$$b = \left[\frac{P_a}{4\pi r_o^2 K L}\left(\frac{1}{2n_o} \frac{dn}{dT} + n_o^2 \alpha C_{r,\phi}\right)\right]^{-1/2} \tag{8}$$

The mirror diameters are $2a_1$ and $2a_2$, respectively, and the corresponding radii of curvatures are R_1 and R_2 which are illustrated in Fig. 20. Then, the stability condition is specified in the following form:

$$-1 < G_1 G_2 < 1 \qquad (9)$$

Table 2 lists the parameters used in the calculation, and Table 3 shows the calculated values of absorbed pump power in crystals, the temperature difference between the center and surface of both Cr:Nd:GSGG and Nd:YAG laser rods, thermal focusing, and resonator stability condition at various CW pump powers densities. The large temperature difference between surface and center of the Gr:Nd:GSGG rod causes severe thermal focusing compared to the Nd:YAG's case even at low pump powers. While the stability condition of the Nd:YAG laser extends up to pump power density of greater than 3,500 solar constants, that of the Cr:Nd:GSGG laser extends only up to 1,500 solar constants. The experimental results agree with these calculations. The distortion of end-face curvature of the rod caused by the radial temperature gradient was neglected in our calculation because both ends of the rod were placed in shadow regions from the pump beam as shown in Fig. 4.

D. Conclusion

A study on Nd:YAG, Nd:YLF and Cr:Nd:GSGG materials has been performed in this research for the solar-pumped laser application. The lowest threshold pump power observed with a 1/8" diameter by 3' long Nd:YLF under a solar-simulator pumping was 129 W which corresponds to the pump beam intensity of 211 solar constants at the rod surface, and a slope efficiency of 0.17 percent was achieved at near threshold region with an output mirror of 95 percent reflectivity. For a Nd:YAG crystal which has the same size as the Nd:YLF, the lowest threshold pump power was 143 W (corresponding intensity of 236 solar constants) and a slope efficiency of 0.12 percent was achieved at near threshold region with an output mirror of 98 percent reflectivity. Since the absorption efficiencies of the crystals are different, specifying the threshold condition of the crystals in terms of the absorbed pump power density is more meaningful in the comparison of crystals. The absorbed threshold pump power densities

corresponding to the above threshold pump powers are 8.1 w/cm^3 for the π-polarization of Nd:YLF, 6.0 w/cm^3 for the σ-polarization of Nd:YLF and 13.5 w/cm^3 for the Nd:YAG. The absorbed threshold pump power density of Nd:YLF is about half of that of Nd:YAG. This is because the absorption efficiency of the Nd:YLF is about half of that of the Nd:YAG. This means that the thickness of the Nd:YLF can be larger than that of Nd:YAG for a given solar pump power. From our measurements it was observed that a 1/4" diameter Nd:YLF provides about 23 percent better slope efficiency and requires 13 percent higher threshold pump power than a 1/8" diameter Nd:YLF does.

In space generally two types of solar collectors, parabolic type and trough type, as shown in Figs. 21 and 22, can be used for the laser pumping. Since the parabolic (or modified parabolic) type collector provides a relatively high solar beam concentration (up to the practical limit of 40,000 solar constants), the lasing medium diameter should be large enough to have an efficient use of the solar beam. However, the lasing medium diameter is limited to the threshold pump power density requirement in the entire volume of the lasing medium. From these considerations the diameter of Nd:YLF can be chosen to be larger than that of Nd:YAG, and the Nd:YLF will provide higher laser output than the Nd:YAG. Problems involved with the large diameter are growth of a such big crystal and a large temperature gradience between rod surface and center. These problems may be solved by having a bundle of thin crystal rods. On the other hand, the trough type collector provides the maximum solar beam concentration of only 200 solar constants. Neither of Nd:YAG and Nd:YLF rods with a 1/8" diameter is suitable for the trough type collector. However, the crystals with a diameter smaller than 1/8" might be useful for this type of collector. Further experimental study on this subject should be due to determine the possibility.

The CW laser operation of the Cr:Nd:GSGG crystal was found to be very difficult with the continuous solar-simulator pumping because of too much thermal lensing effect caused by a large amount of the pump beam absorption in the crystal. The true CW laser operation of the Cr:Nd:GSGG was observed for pump power densities up to 1500 solar constants (=230 W/cm^2). For pump power densities from 1,500 solar constants to 2,500 solar constants (=338 W/cm^2) a quasi CW laser operation was

demonstrated. The difficulty of the CW laser operation of the Cr:Nd:GSGG crystal was also observed by Barnes, et al., in Ref. 3. Our calculation shows that the amount of solar beam absorption by the Cr:Nd:GSGG is about 6 times larger than that by the Nd:YAG for the same incoming beam and the thermal focusing of the Cr:Nd:GSGG is more than 10 times greater than that of the Nd:YAG. The crystal was damaged by thermal cracking when the quasi CW laser operation was performed at a pump power density of about 3,000 solar constants (=405 W/cm^2) for several minutes. We found that better solar-pumped laser performance of the Cr:Nd:GSGG over the Nd:YAG expected in Ref. 2 may be difficult to realize. However, the laser performance of the Cr:Nd:GSGG crystal with a small diameter should be further investigated under low pump power densities of the possible use with the trough type collector, and the use of a fiber bundle of the crystal in the parabolic type collector should be also investigated for a high power application.

E. Appendix

According to Refs. 20 and 21 the ray matrix relating the output ray (x_2, x_2') to the input ray (x_o, x_o') in a lens like medium whose refractive index n varies near optic axis as in $n = n_o(1 - 2 r^2/b^2)$ is written as

$$\begin{vmatrix} x_2 \\ x_2' \end{vmatrix} = \begin{vmatrix} 1 & 0 \\ 0 & n_o \end{vmatrix} \begin{vmatrix} x_1 \\ x_1' \end{vmatrix}$$

$$= \begin{vmatrix} 1 & 0 \\ 0 & n_o \end{vmatrix} \begin{vmatrix} \cos(2L/b) & (b/2)\sin(2L/b) \\ -(2n_o/b)\sin(2L/b) & n_o\cos(2L/b) \end{vmatrix} \begin{vmatrix} x_o \\ x_o' \end{vmatrix}$$

where n is a constant, b is the measure of the degree of the variation of n and L is the distance between the input and output ray points in the lenslike medium. For the resonator shown in Fig.20 the output ray (x_3, x_3') at the output mirror is related to the input ray (x_o, x_o') by the combination of the above ray matrix and a ray matrix in a free space:

$$\begin{vmatrix} x_3 \\ x_3' \end{vmatrix} = \begin{vmatrix} 1 & d \\ 0 & 1 \end{vmatrix} \begin{vmatrix} x_2 \\ x_2' \end{vmatrix}$$

$$= \begin{vmatrix} 1 & d \\ 0 & 1 \end{vmatrix} \begin{vmatrix} \cos(2L/b) & (b/2)\sin(2L/b) \\ -(2n_o/b)\sin(2L/b) & n_o\cos(2L/b) \end{vmatrix} \begin{vmatrix} x_o \\ x_o' \end{vmatrix}$$

$$= \begin{vmatrix} \cos(2L/b)-(2n_od/b)\sin(2L/b) & (b/2)\sin(2L/b)+ n_od\cos(2L/b) \\ -(2n_o/b)\sin(2L/b) & n_o\cos(2L/b) \end{vmatrix} \begin{vmatrix} x_o \\ x_o' \end{vmatrix}$$

$$= \begin{vmatrix} A & B \\ C & D \end{vmatrix} \begin{vmatrix} x_o \\ x_o' \end{vmatrix}$$

where
$A = \cos(2L/b) - (2n_od/b)\sin(2L/b)$
$B = (b/2)\sin(2L/b) + n_od\cos(2L/b)$
$C = -(2n_o/b)\sin(2L/b)$
$D = n_o\cos(2L/b)$

Thus, the focal length of the lenslike medium is written as

$$f = -1/C = [(2n_o/b)\sin(2L/b)]^{-1}$$

and G parameters of the optical resonator shown in Fig.4 are written as

$$G_1 = (a_1/a_2)(A - B/R_1)$$

$$= (a_1/a_2)[\cos(2L/b)-(2n_od/b)\sin(2L/b) - \{(b/2)\sin(2L/b)+ n_od\cos(2L/b)\}/R_1]$$

$$G_2 = (a_2/a_1)(D - B/R_2)$$

$$= (a_2/a_1)[n_o\cos(2L/b) - \{(b/2)\sin(2L/b)+n_od\cos(2L/b)\}/R_2]$$

Reference

1. K. S. Han, K. H. Kim and L. V. Stock, "Evaluation of Solid-State Laser Materials for Solar Pumping," pp. 11-69 in NASA Contractor Report #180541 entitled Direct Solar-Pumped Iodine Laser Amplifier (1987).

2. M. Weksler and J. Shwartz, "Solar-Pumped Solid State Laser," SPIE Vol. 736, New Slab and Solid-State Laser Technologies and Applications, 84 (1987).

3. N. P. Barnes, D. J. Gettemy, L. Esterowitz and R. E. Allen, "Comparison of Nd 1.06 and 1.33 μm Operation in Various Hosts," IEEE J. Quantum Electron, QE-23(9), 1434 (1987).

4. A. L. Harmer, A. Linz and D. R. Gabbe, "Fluroescence of Nd^{+3} in Lithium Yttrium Fluoride," J. Phys. Chem. Solids, 30, 1483 (1969).

5. E. J. Sharp, D. J. Horowitz ad J. E. Miller, "High-Efficiency Nd^{+3}:$LiYF_4$ Laser," J. Appl. Phys. 44(12), 5399 (1973).

6. D. LeGoff, A. Bettinger and a. Labadens, "Etude Dun Oscillateur a Blocage De Modes Utilisant un Crystal Dd $LiYF_4$ Dope au Neodyme," Opt. Commun. 26(1), 108 (1978).

7. H. P. Jenssen, D. R. Gabbe, A. Linz, and O. S. Naiman, "Spectral Diversity Crystalline Fluoride Lasers," proc. of the International Conf. on Lasers '81, 735 (1981).

8. T. M. Pollak, W. F. Wing, R. J. Grasso, E. P. Chicklis and H. P. Jenssen, "CW Laser Operation of Nd:YLF," IEEE J. Quantum Electron, GE-18(2), 159 (1982).

9. J. C. McCarthy, M. G. Knights and E. P. Chicklis, "Laser Performance of Nd:YLF," SPIE vol. 335, Advanced Laser Technology and Applications, 2(1982).

10. J. E. Murray, "Pulsed Gain and Thermal Lensing of Nd:$YiYF_4$," IEEE J. Quantum Electron. QE-19(4), 488 (1983).

11. M. D. Thomas, M. G. Knights and E. P. Chicklis, "High Gain Nd:YLF Amplifier," SPIE vol. 622 High Power and Solid State Lasers, 142(1986).

12. R. A. Brandewie and C. L. Telk, "Quantum Efficiency of Nd^{3+} in Glass, Calcium Tungstate,and Yttrium Aluminum Garnets" J. Opt. Soc. Am., 57(10), 1221 (1967).

13. W. Koechner, "Solid State Laser Engineering," Springer-Verlag, New York (1976), pp.57.

14. J. A. Williams, PRC/Kentron Inc., NASA Langley Research Center Private Communication.

15. D. D. Bhawalker and L. Pandit, "Improving the Pump Efficiency of a Nd^{3+}:Glass Laser Using Dyes," IEEE J. Quantum Electron., QE-9(1), 43 (1973).

16. W. Koechner, "Solid State Laser Engineering," Springer-Verlag, New York, (1987), Chap. 7 and reference there in.

17. J. D. Foster and L. M. Osterink, "Thermal Effects in a Nd:YAG Laser," J. Appl. Phys., 41(9) 3656 (1970).

18. Allied Corporation Synthetic Crystal Products; Data Sheet, P. O. Box 31428 Charlotte, North Carolina 28231 (1986).

19. W. F. Krupke, M. D. Shinn, J. E. Marion, J. A. Caird, and S. E Stokowskii, "Spectroscopic, Optical, and Thermomechanical Properties of Neodymium- and Chromium-doped Gadolinium Scandium Gallium Garnet," J. Opt. Soc. Am. B, 3(1), 102 (1986).

20. H. Kogelnik, BSTJ 44, 455 (1965).

21. A. Yariv, "Quantum Electronics," 2nd ed. John Wiley & Sons, New York (1975), Chapter 6.

Figure 1. Experimental setup to measure the solar-simulator's beam intensity distribution measurement inside transparent or diffused glass tubes.

Figure 2. The distribution of the solar-simulator beam intensity at the surface of 3.2 mm crystal rod which was placed along the collector cone axis and covered with various glass tubes. The solar-simulator's input current used was 200 A.

Figure 3. The solar simulator's beam intensity at the 3.2 mm crystal rod surface as a function of the input current.

Figure 4. Experimental setup used for CW (or quasi CW) laser operation of the 3 crystals with a solar-simulator as a pumping source. PD: silicon photodiode.

Figure 5. The absorption spectrum of the 1.1 at % Nd:YAG crystal including the background absorption compared with the spectral irradiance of the air-mass-zero solar spectrum.

Figure 6. The absorption spectrum of Cr:Nd:GSGG with doping densities of Cr^{3+} = 2 x 10^{20} ions/cm^3 and Nd^{3+} = 2 x 10^{20} ions/cm^3 including the background absorption compared with the spectral irradiance of the air-mass-zero solar spectrum.

Figure 7. The absorption spectrum of 1.5 at % Nd:YFL (π-polarized)crystal compared with the spectral irradiance of the air-mass-zero solar spectrum.

Figure 8. The absorption spectrum of 1.5 at % Nd:YLF (σ-polarized)crystal compared with the spectral irradiance of the air-mass-zero solar spectrum.

Figure 9. CW laser outputs from the Nd:YAG and Nd:YLF crystals with various output coupling mirrors and with various solar-simulator's pump powers. Three different output mirrors were used in this measurement, and each had a curvature of 0.3 m.

Figure 10. The CW laser output of Nd:YAG with various output coupling mirrors as a function of input pump power. The percent values shown in the figure are the reflectance of the mirrors at 1.06 μm , and the following values are the radii of the curvature of the mirrors.

Figure 11. The CW laser output of a 1/8" diameter and 3" long Nd:YLF rod with two different output mirrors as a function of input pump power. The numbers shown beside the data points are the mirror reflectance and radius of curvature.

Figure 12. The CW laser output from two different diameters of Nd:YLF rods which have the same length (3 inches) as a function of pump power at near thereshold region. The data was taken with three different glass tubes for the water jacket shown in Figs. 4 and 5.

Figure 13. The CW laser output from two different diameters of Nd:YLF rods, both of which have the same length of 3 inches, as a function of pump power. The data was taken with a transparent glass tube for the water jacket shown in Fig. 4.

Figure 14. The CW laser output from a 1/8" diameter Nd:YLF rod as a function of pump power with water circulation and with dye circulation in the cooling jacket. The glass tube used in this measurement had 13 mm outer diameter and 11 mm inner diameter. See text for discussion on these data.

Figure 15. CW laser output powers of the Nd:YAG and Nd:YLF crystals and average power of the quasi-CW laser output of the Cr:Nd:GSGG crystal at various pump powers. Comparison among the crystals may not be made from this drawing. See text for reason. The size of each crystal rod was 1/8" thick and 3" long.

Figure 16. Experimental setup for flashlamp experiment. A 1.3 μF capacitor was used along with the power supply. PD: silicon photodiode, ND: neutral density filter and BS: beam splitter.

Figure 17. The output energy of the flashlamp-pumped Nd:YLF laser with various output coupling mirrors as a function of the electrical input energy.

Figure 18. Flashlamp-pumped Cr:Nd:GSGG laser output with various output mirrors as a function of input energy. The scales are not comparable with the ones in Figs. 17 and 19 because the experimental condition was changed.

Figure 19. Flashlamp-pumped Cr:Nd:GSGG laser output with various output mirrors as a function of low input energy. The x-axis scale should not be compared with that in Fig. 18 because the experimental condition was changed.

Figure 20. A diagram showing ray positions (x) and directions (x') with respect to the central axis line at various positions in the laser cavity used in our experiment 2a, and $2a_2$ are the diameters of the mirrors, and R_1 and R_2 are the radii of the mirror curvatures.

Figure 21. Solar-pumped laser system with a parabolic collector.

Figure 22. Solar-pumped laser-amplifier system with a trough type of collector.

Table 1 Comparison of the solar-simulator pumped laser output of Nd:YLF with that of Nd:YAG

	Slope Eff.	Threshold Pump Power (Intensity)	Absorbed Threshold Pump Power Density	Slope Eff.	Threshold Pump Power (Intensity)	Absorbed Threshold Pump Power Density
95% Mirror	0.17%	258W (424 SC)	16.3W/cm^3 (π-pol) 12.0 (σ-pol)	0.085%	261W (429 SC)	24.7 W/cm^3
98% Mirror	0.13%	167W (275 SC)	10.5W/cm^3 (π-pol) 7.8 (σ-pol)	0.12%	181W (297 SC)	17.1 W/cm^3
Rmax Mirror	0.01%	129W (211 SC)	8.1 W/cm^3 (π-pol) 6.0 (σ-pol)	0.01%	143W (236 SC)	13.5 W/cm^3

Table 2. Thermal and Physical Parameters of Cr:Nd:GSGG and Nd:YAG

	Cr:Nd:GSGG	Nd:YAG	Reference
n_o	1.95	1.82	18
α ($\times 10^{-6}$/K)	7.5	7.5	18
dn/dT ($\times 10^{-6}$/K)	10.1	7.3	18
K (W/cm.K)	0.06	0.14	18
C_r	0.024	0.0196	19
C_ϕ	0.0015	-0.0025	19
r_o (cm)	0.16	0.16	
L (cm)	7.62	7.62	
a_1 (cm)	0.16	0.16	
a_2 (cm)	1.27	1.27	
R_1 (cm)	500	500	
R_2 (cm)	30	30	
d (cm)	9.0	9.0	
ξ	0.02	0.02	
ℓ (cm)	0.343	0.347	
λ_1 (nm)	300	300	
λ_2 (nm)	900	900	

Note: 1. The rod length L was replaced in the absorbed pump power calculations with the length of rod exposed to the pump light which is about 6.9 cm.

2. The value for reflective loss coefficient, ξ, at the rod surface was approximated.

3. The path length of the pump beam in the crystal is calculated as $\ell = 2r_o/\cos[\sin^{-1}(\sin 45^\circ/n_o)]$ for a 45° incident light.

Table 3. Absorbed pump power in the crystal, temperature difference between center and surface of laser rod, thermal focus, and stability condition.

SOLAR CONSTANT	ABSORBED POWER(W)	T(0)-T(R) (degree)	Fr (cm)	Fϕ (cm)	G1·G2	STABILITY CONDITION
Cr:Nd:GSGG						
1000	330.21	57.47	3.10		-.45	STABLE
				3.62	-.70	STABLE
1500	495.32	86.21	2.44		.74	STABLE
				2.75	-.03	STABLE
2000	660.42	114.95	2.20		2.21	UNSTABLE
				2.37	1.05	UNSTABLE
2500	825.53	143.69	2.15		3.52	UNSTABLE
				2.20	2.24	UNSTABLE
3000	990.64	172.42	2.24		4.44	UNSTABLE
				2.15	3.31	UNSTABLE
Nd:YAG						
1000	55.21	4.12	45.66		.69	STABLE
				58.36	.75	STABLE
1500	82.82	6.18	30.68		.56	STABLE
				39.15	.64	STABLE
2000	110.42	8.24	23.19		.43	STABLE
				29.54	.54	STABLE
2500	138.03	10.30	18.70		.32	STABLE
				23.78	.45	STABLE
3000	165.64	12.36	15.71		.21	STABLE
				19.94	.36	STABLE

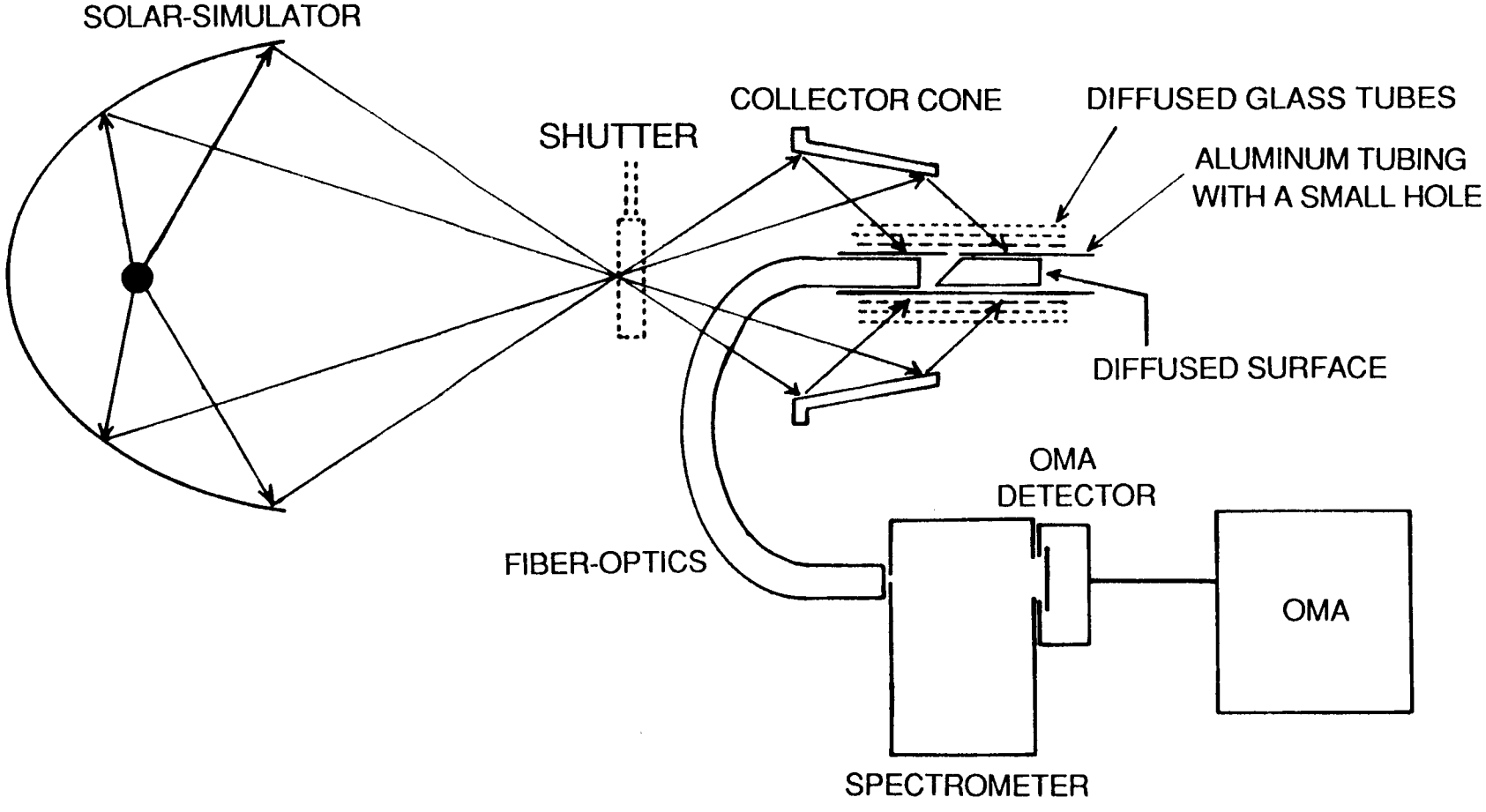

Figure 1. Experimental setup to measure the solar-simulator's beam intensity distribution measurement inside transparent or diffused glass tubes.

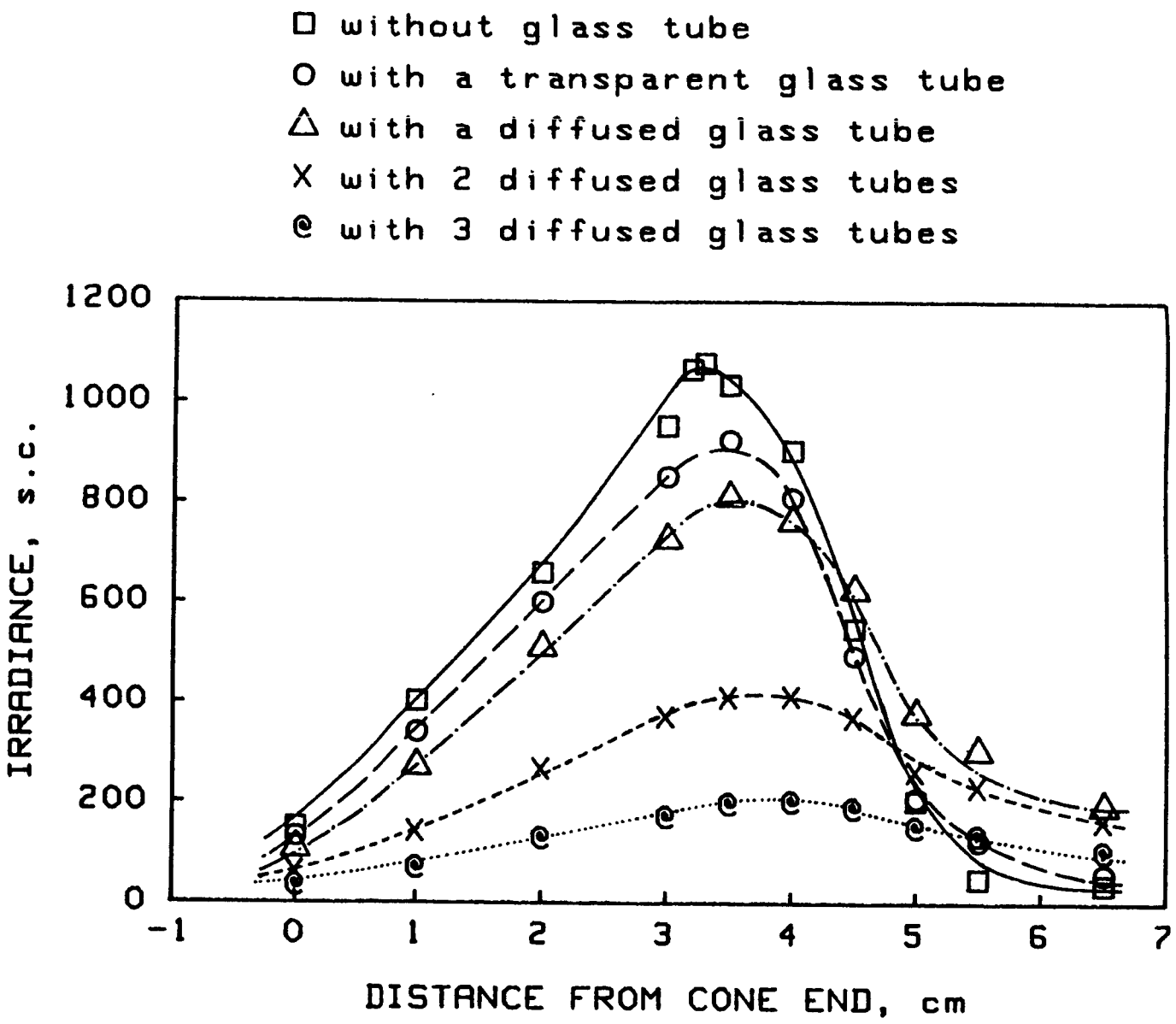

Figure 2. The distribution of the solar-simulator beam intensity at the surface of 3.2 mm crystal rod which was placed along the collector cone axis and covered with various glass tubes. The solar-simulator's input current used was 200 A.

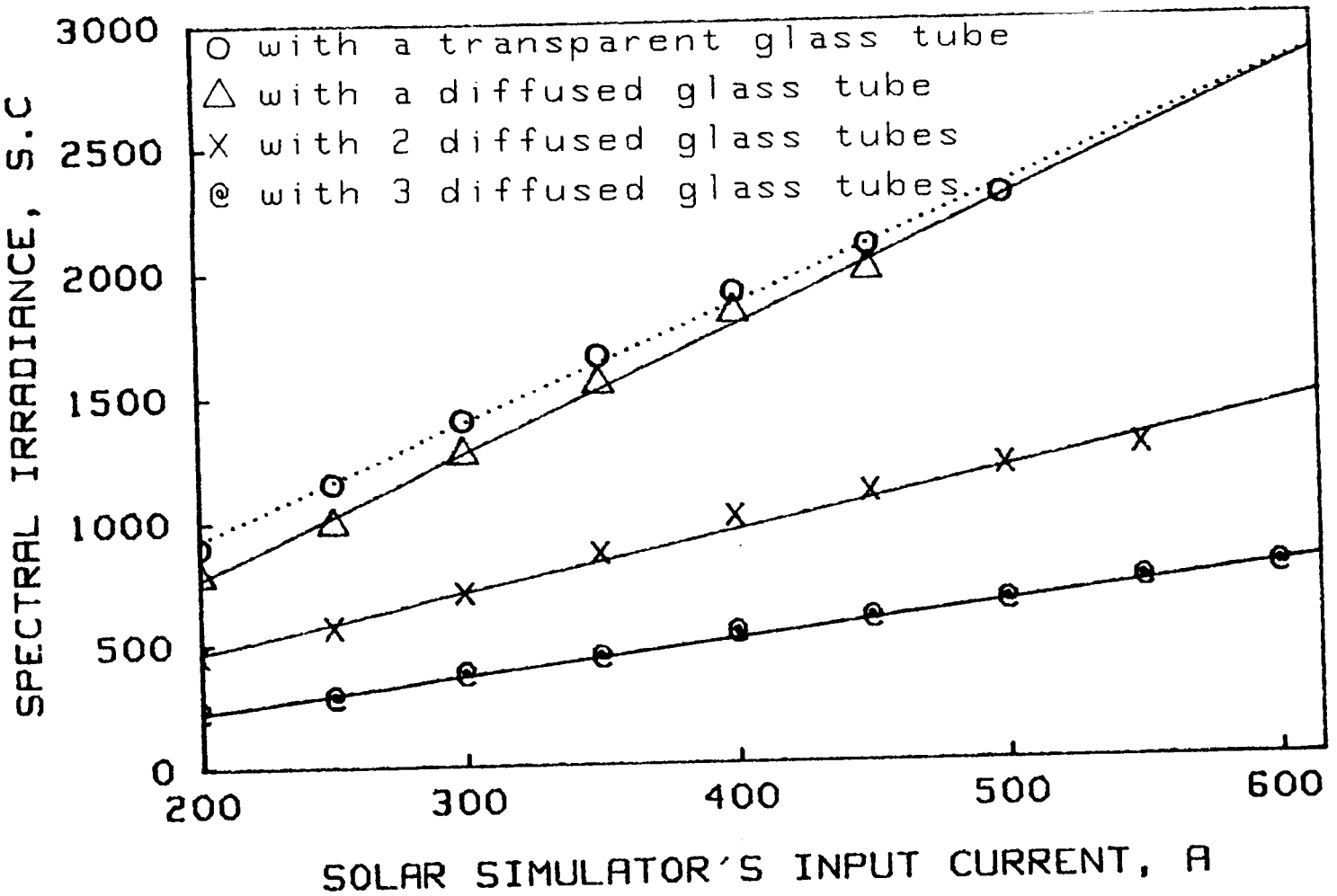

Figure 3. The solar simulator's beam intensity at the 3.2 mm crystal rod surface as a function of the input current.

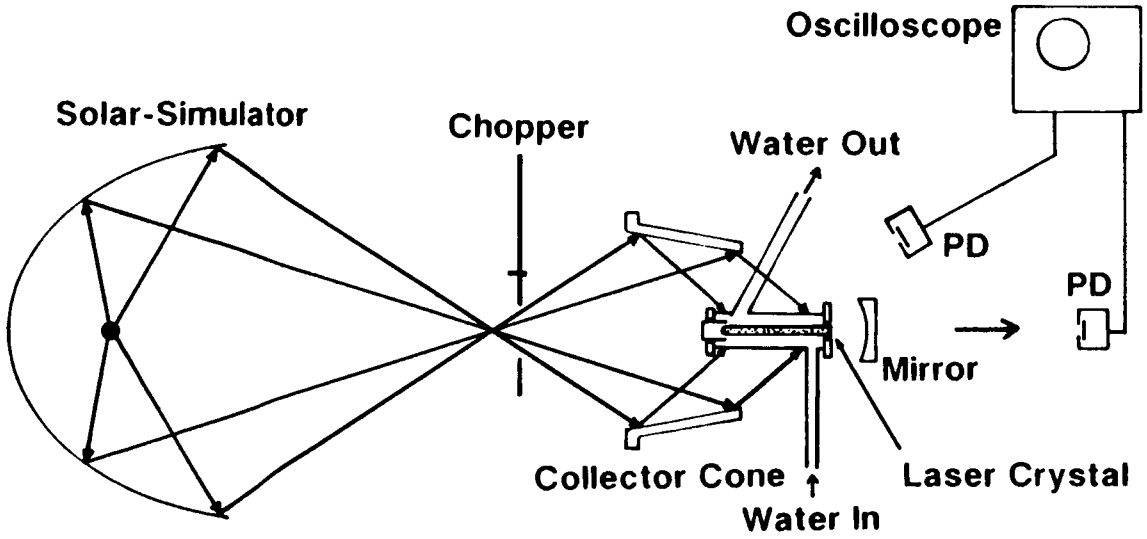

Figure 4. Experimental setup used for CW (or quasi CW) laser operation of the 3 crystals with a solar-simulator as a pumping source. PD: silicon photodiode.

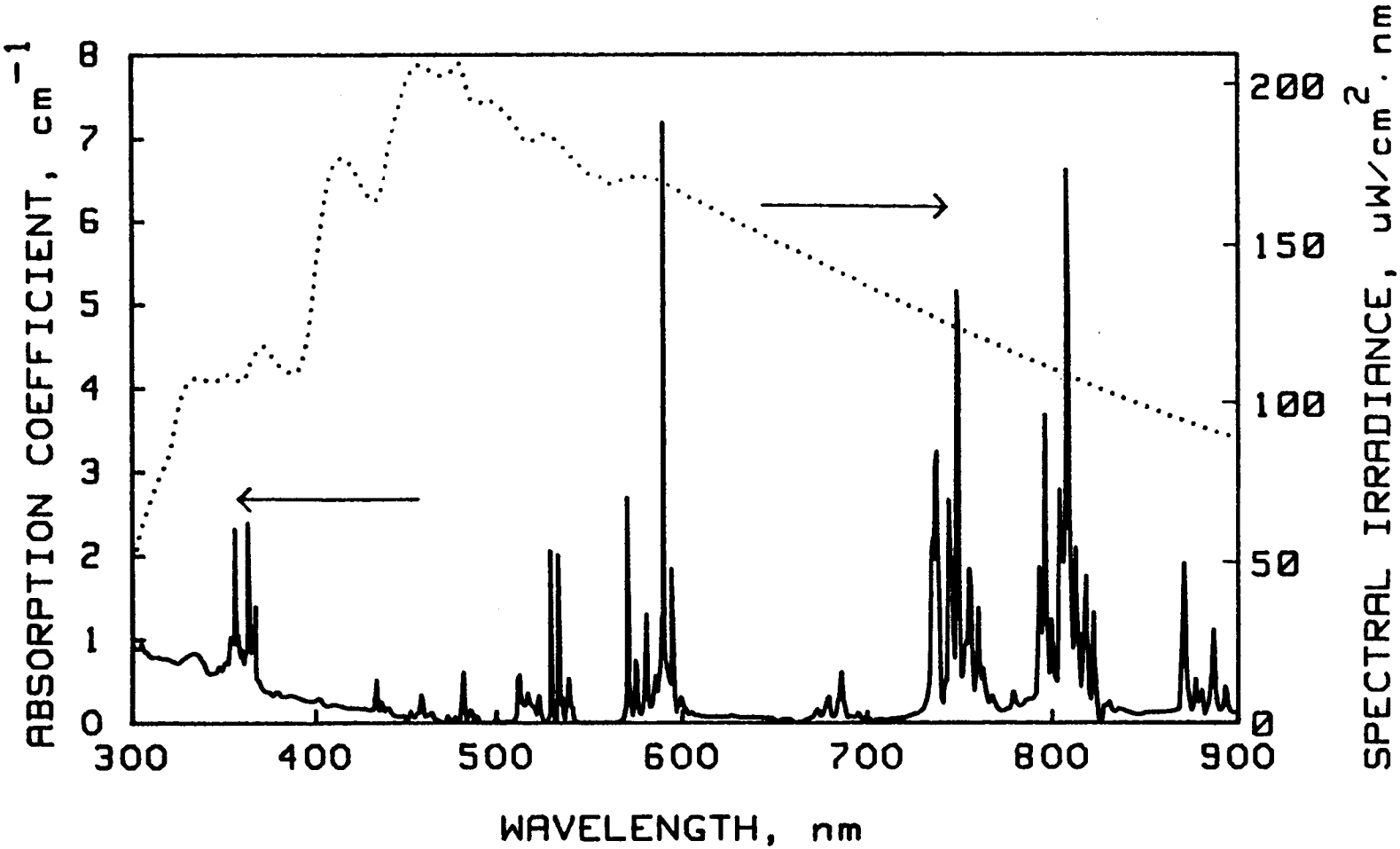

Figure 5. The absorption spectrum of the 1.1 at % Nd:YAG crystal including the background absorption compared with the spectral irradiance of the air-mass-zero solar spectrum.

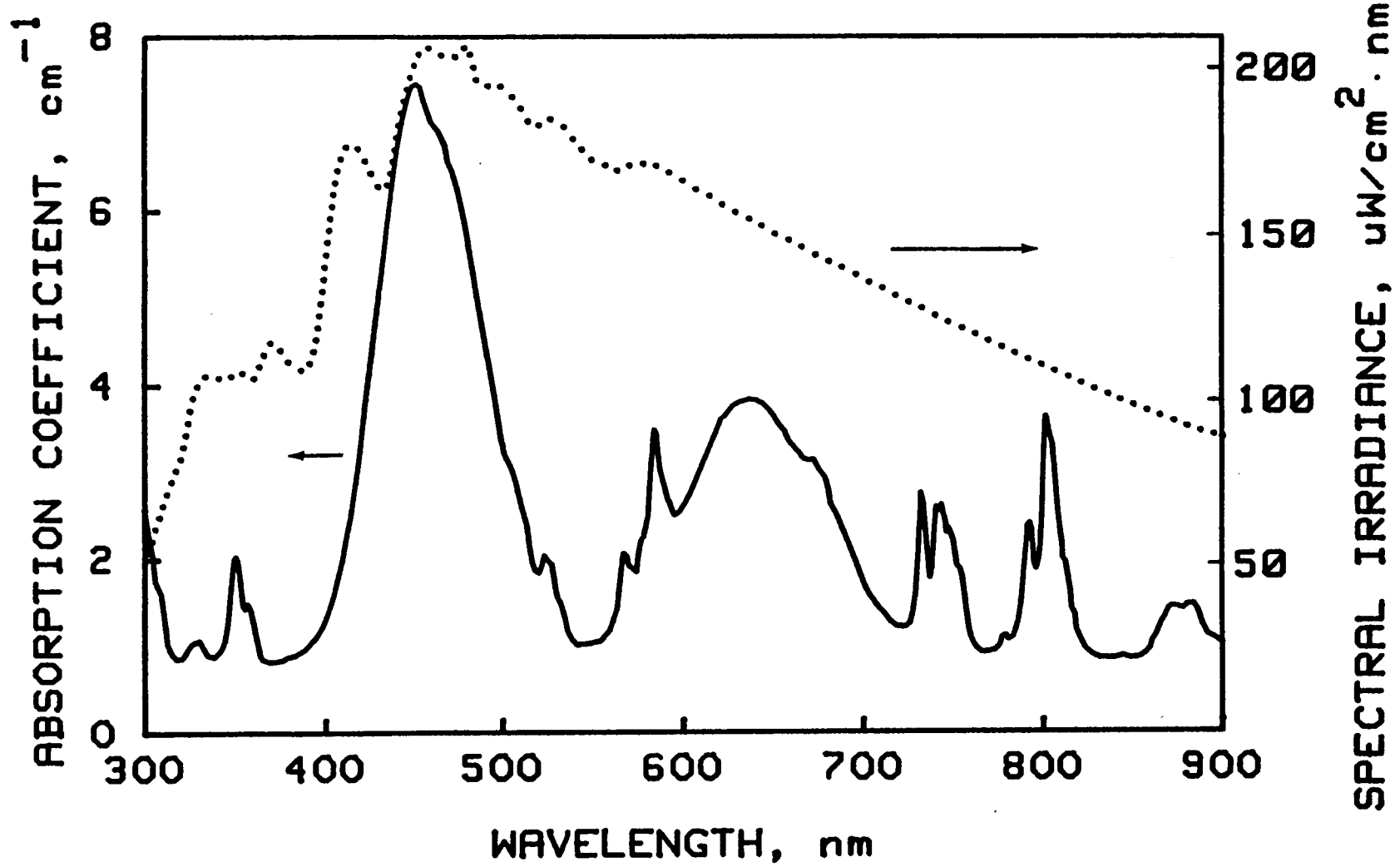

Figure 6. The absorption spectrum of Cr:Nd:GSGG with doping densities of Cr^{3+} = 2 x 10^{20} ions/cm^3 and Nd^{3+} = 2 x 10^{20} ions/cm^3 including the background absorption compared with the spectral irradiance of the air-mass-zero solar spectrum.

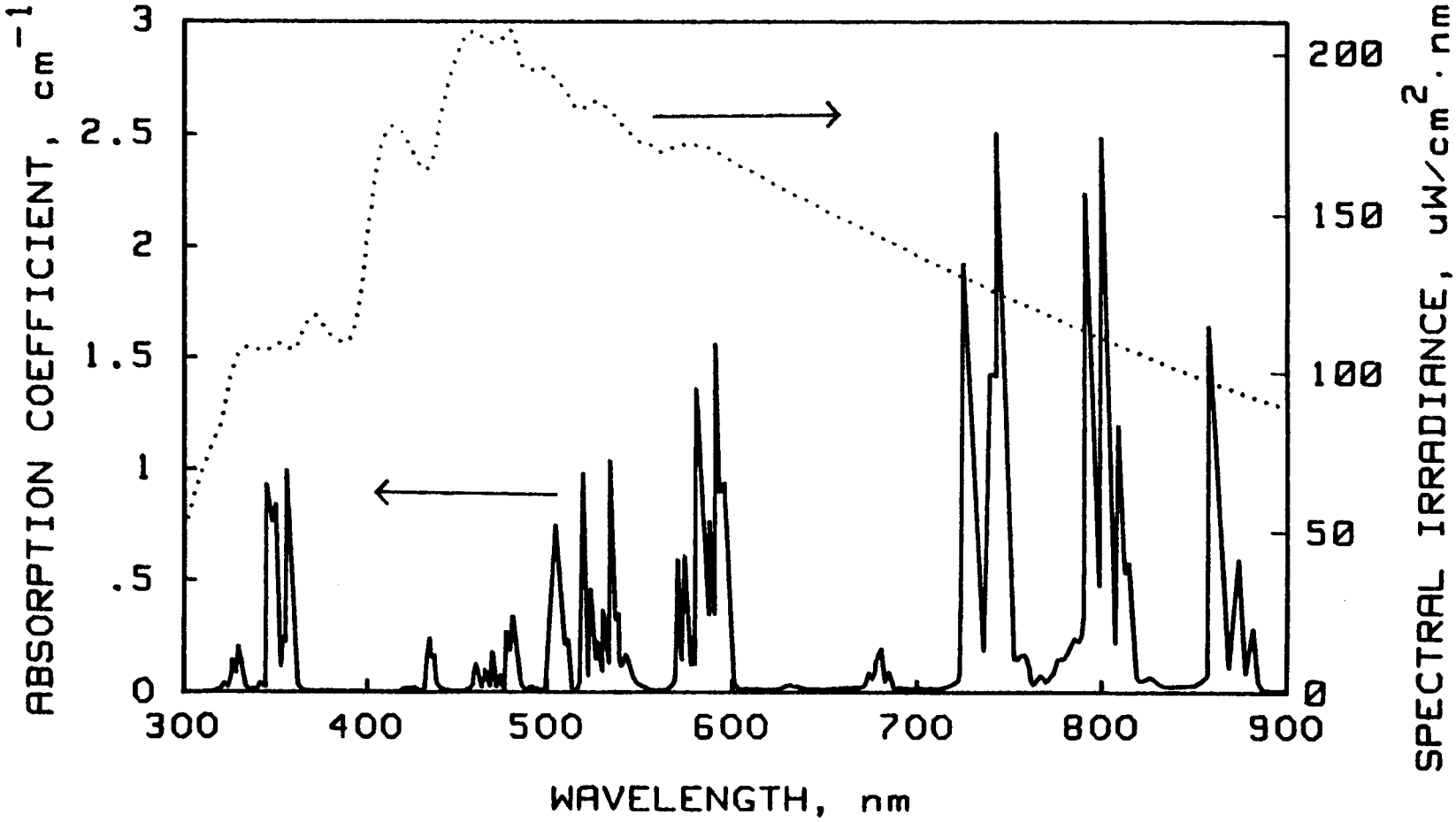

Figure 7. The absorption spectrum of 1.5 at % Nd:YLF (π-polarized) crystal compared with the spectral irradiance of the air-mass-zero solar spectrum.

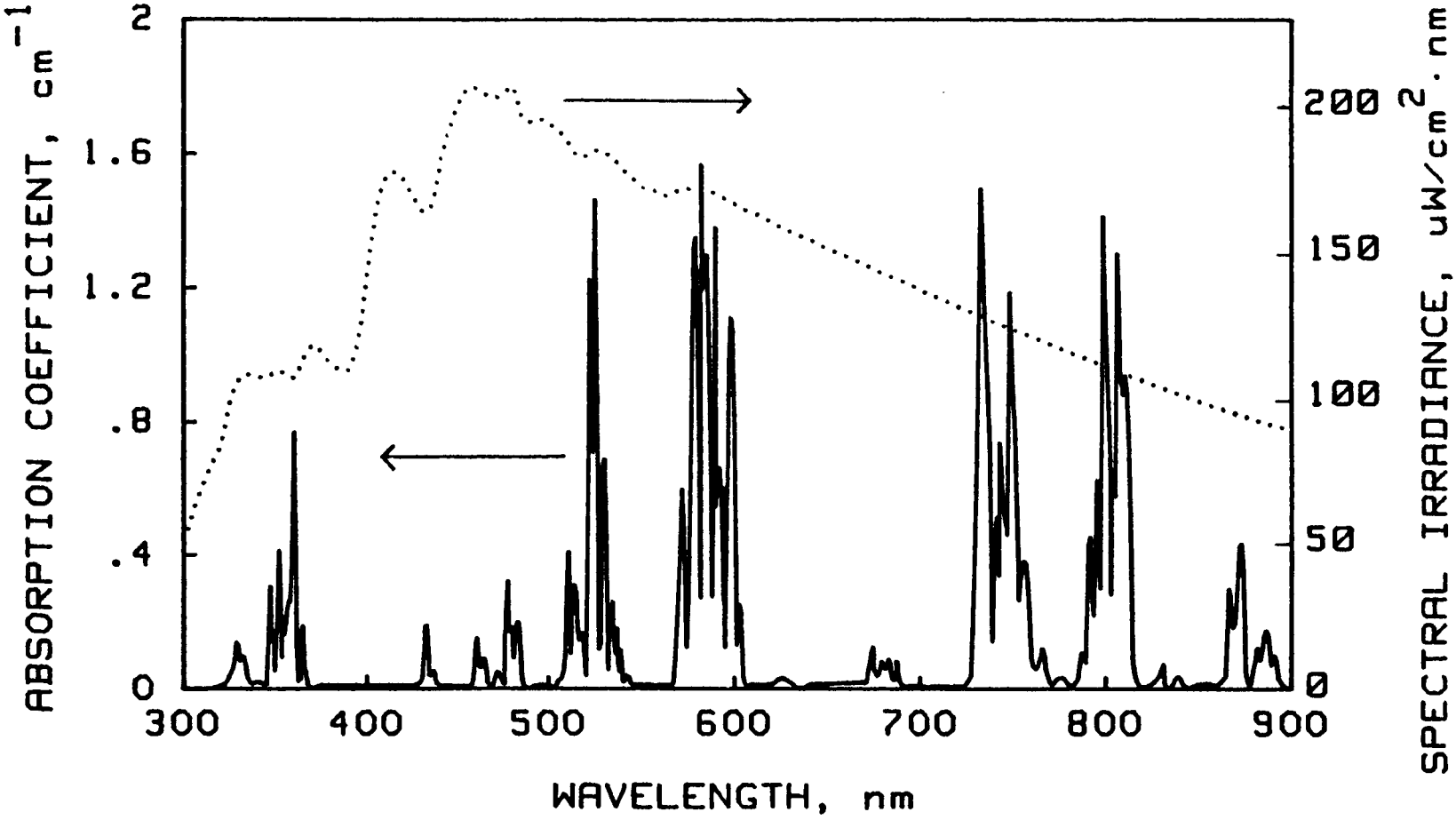

Figure 8. The absorption spectrum of 1.5 at % Nd:YLF (σ-polarized) crystal compared with the spectral irradiance of the air-mass-zero solar spectrum.

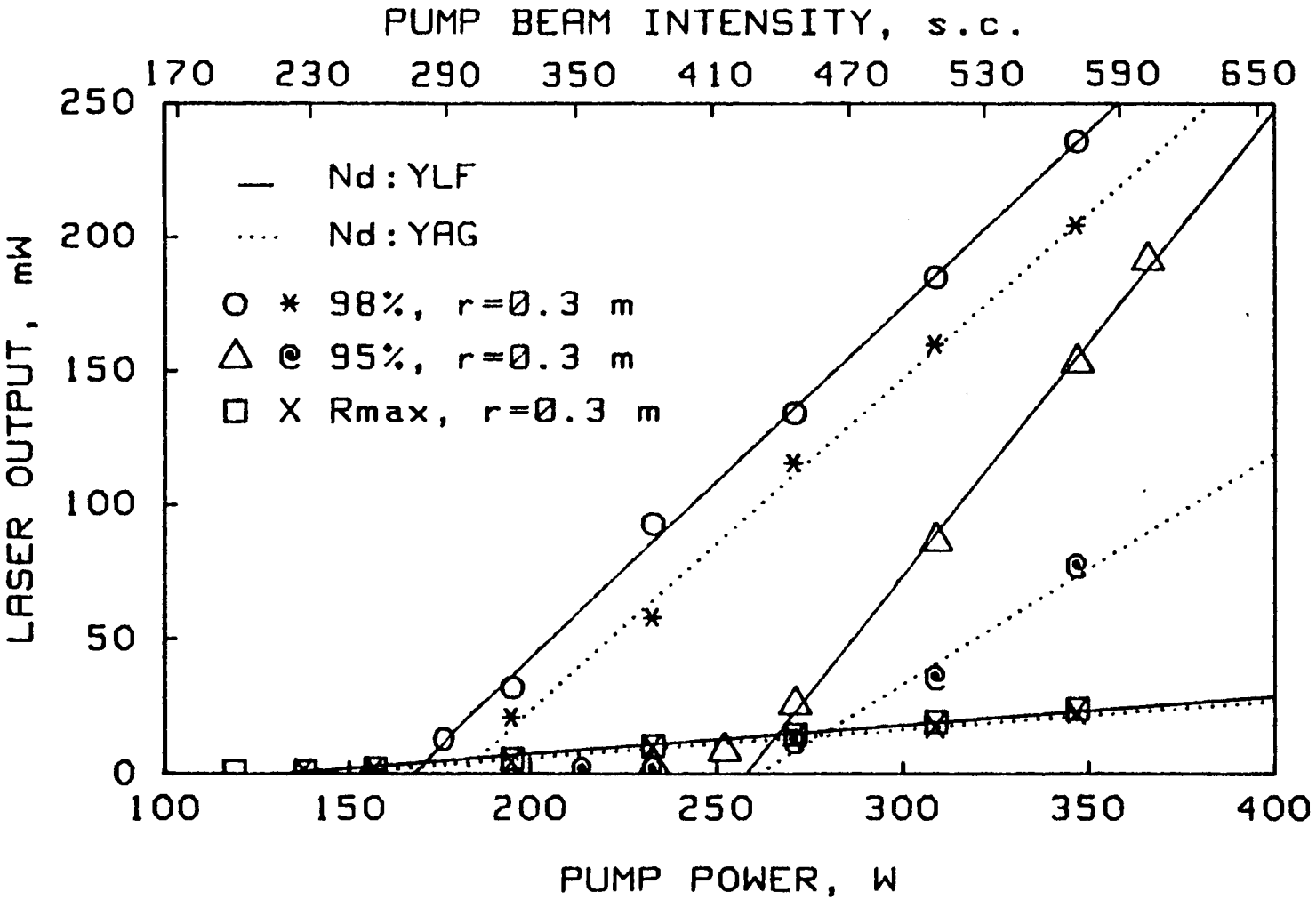

Figure 9. CW laser outputs from the Nd:YAG and Nd:YLF crystals with various output coupling mirrors and with various solar-simulator's pump powers. Three different output mirrors were used in this measurement, and each had a curvature of 0.3 m.

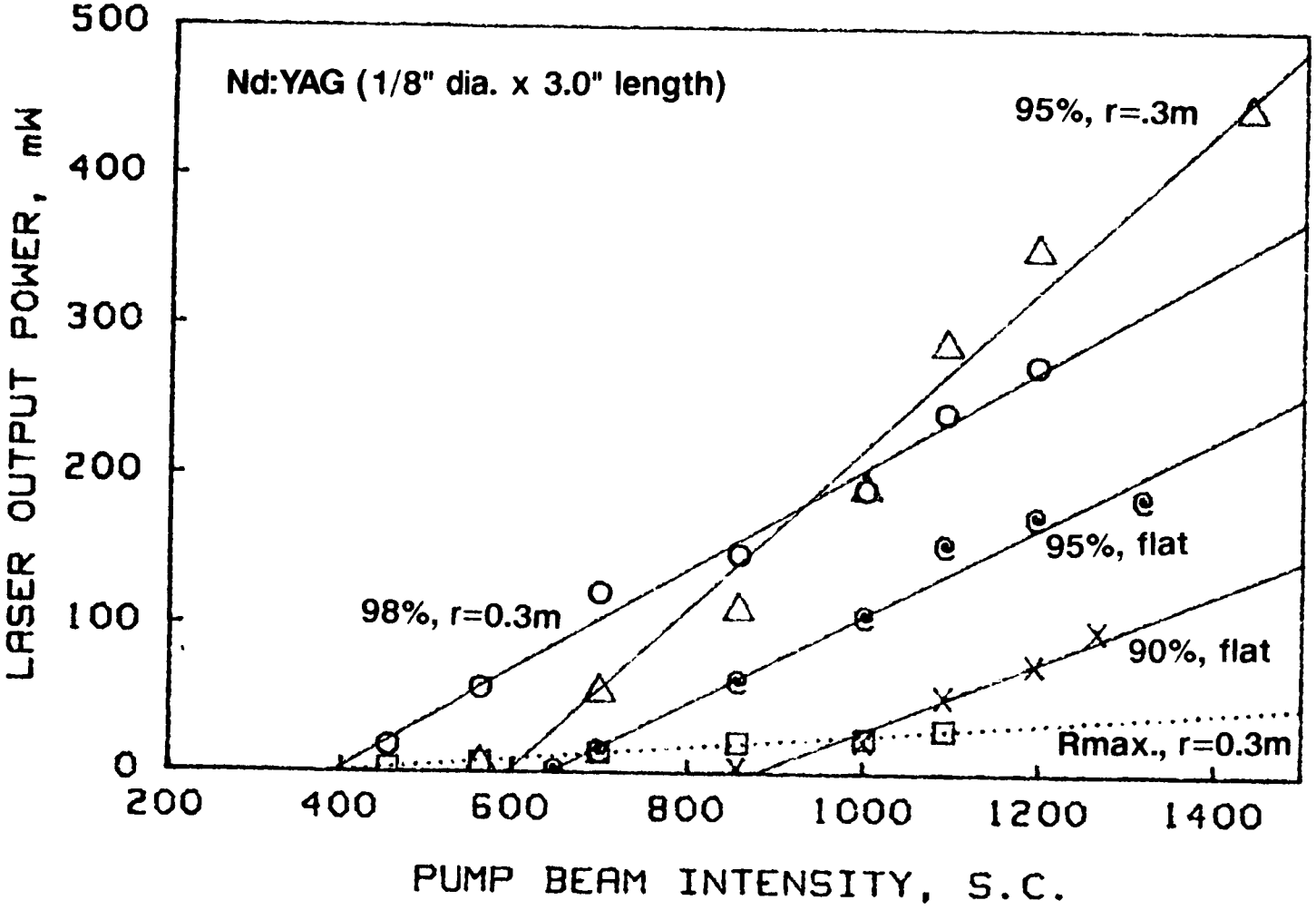

Figure 10. The CW laser output of Nd:YAG with various output coupling mirrors as a function of input pump power. The percent values shown in the figure are the reflectance of the mirrors at 1.06 μm , and the following values are the radii of the curvature of the mirrors.

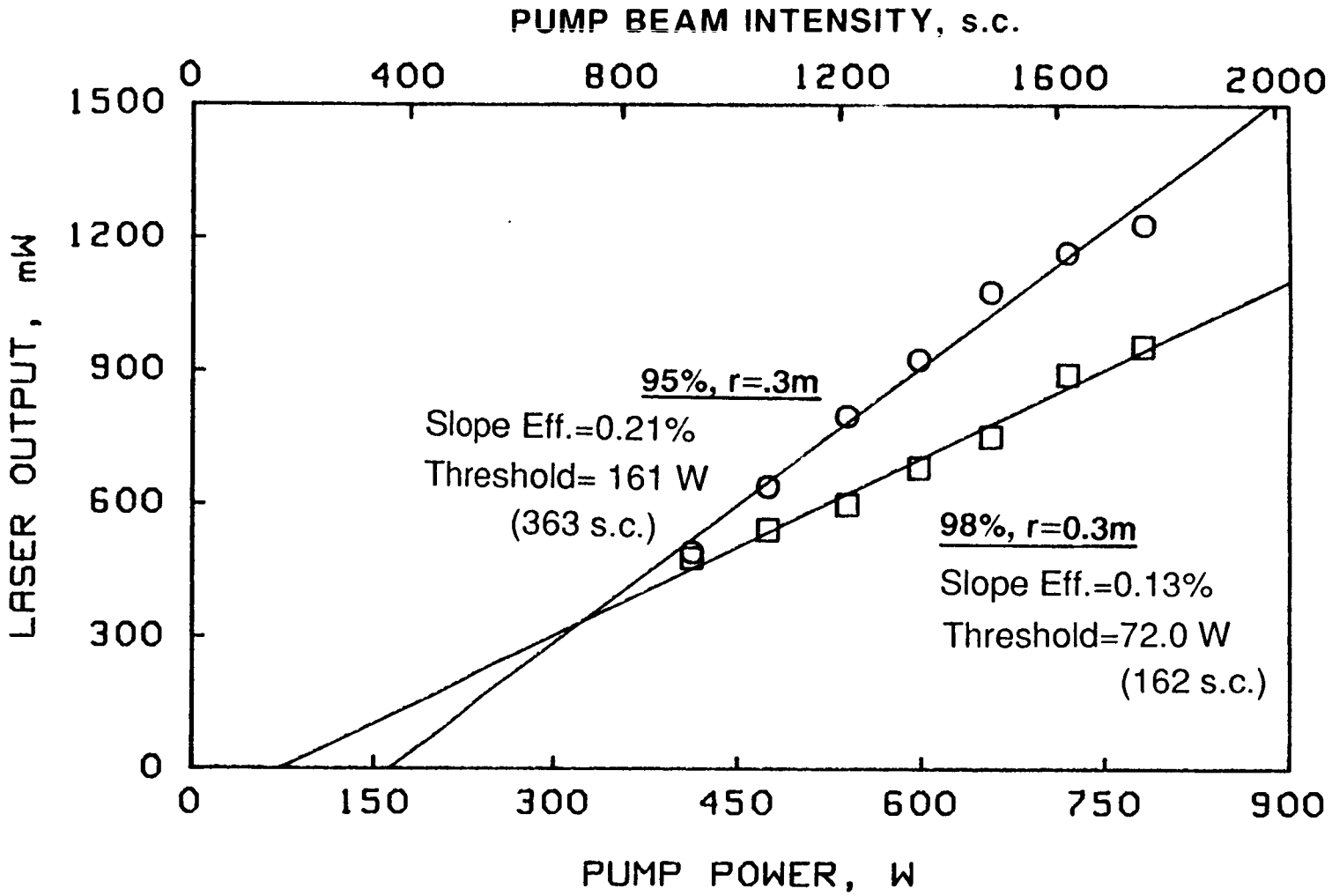

Figure 11. The CW laser output of a 1/8" diameter and 3" long Nd:YLF rod with two different output mirrors as a function of input pump power. The numbers shown beside the data points are the mirror reflectance and radius of curvature.

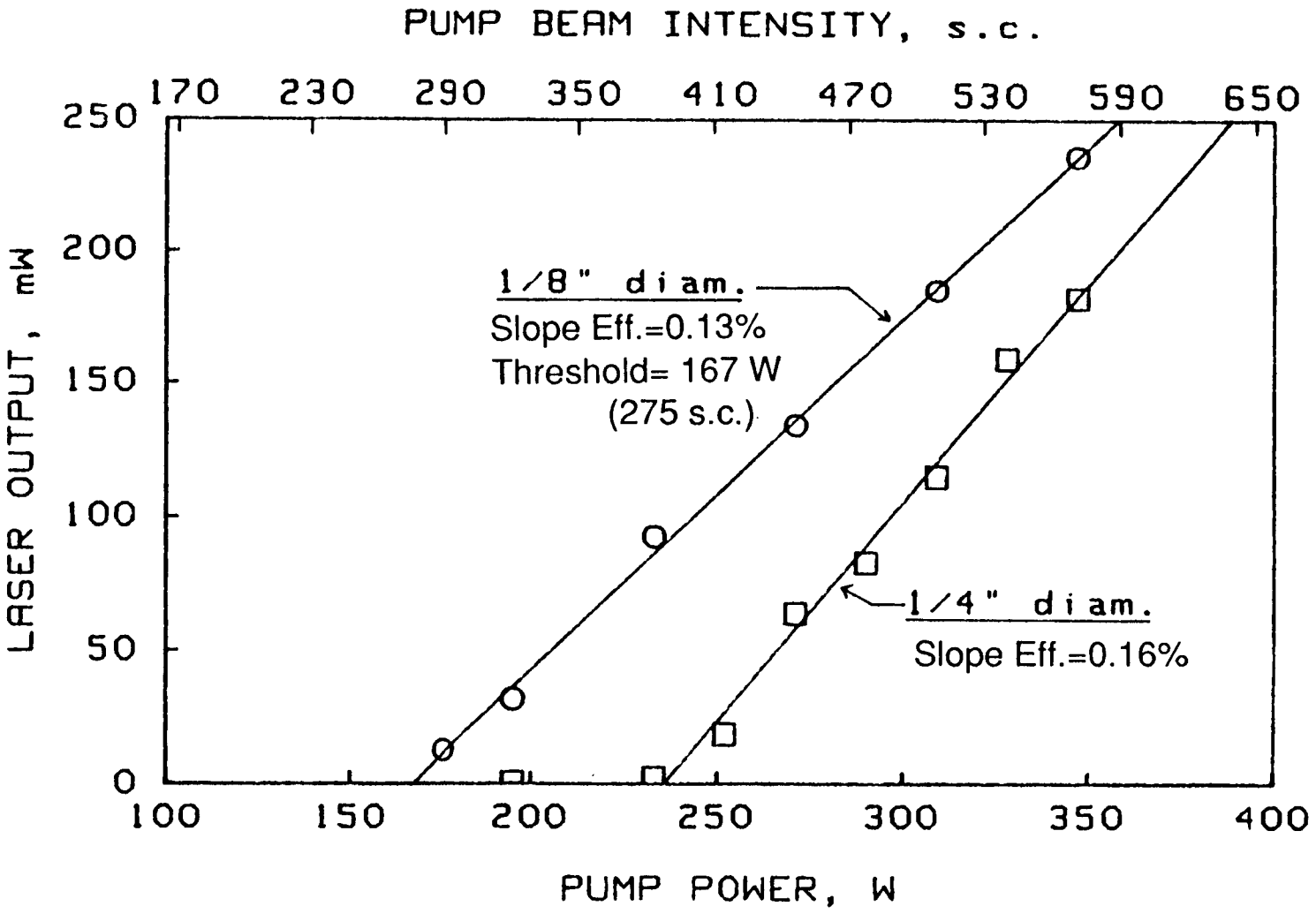

Figure 12. The CW laser output from two different diameters of Nd:YLF rods which have the same length (3 inches) as a function of pump power at near thereshold region. The data was taken with three different glass tubes for the water jacket shown in Figs. 4 and 5.

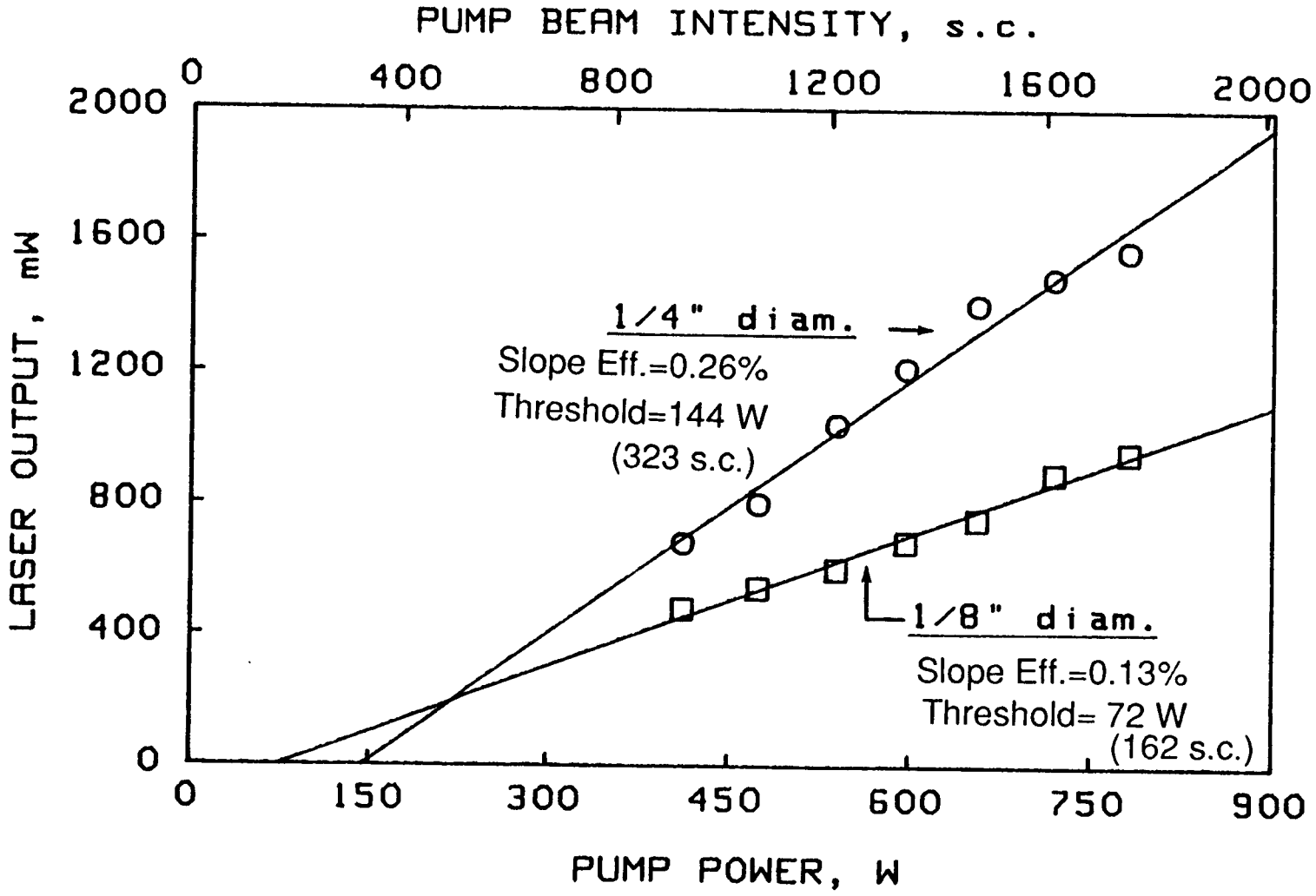

Figure 13. The CW laser output from two different diameters of Nd:YLF rods, both of which have the same length of 3 inches, as a function of pump power. The data was taken with a transparent glass tube for the water jacket shown in Fig. 4.

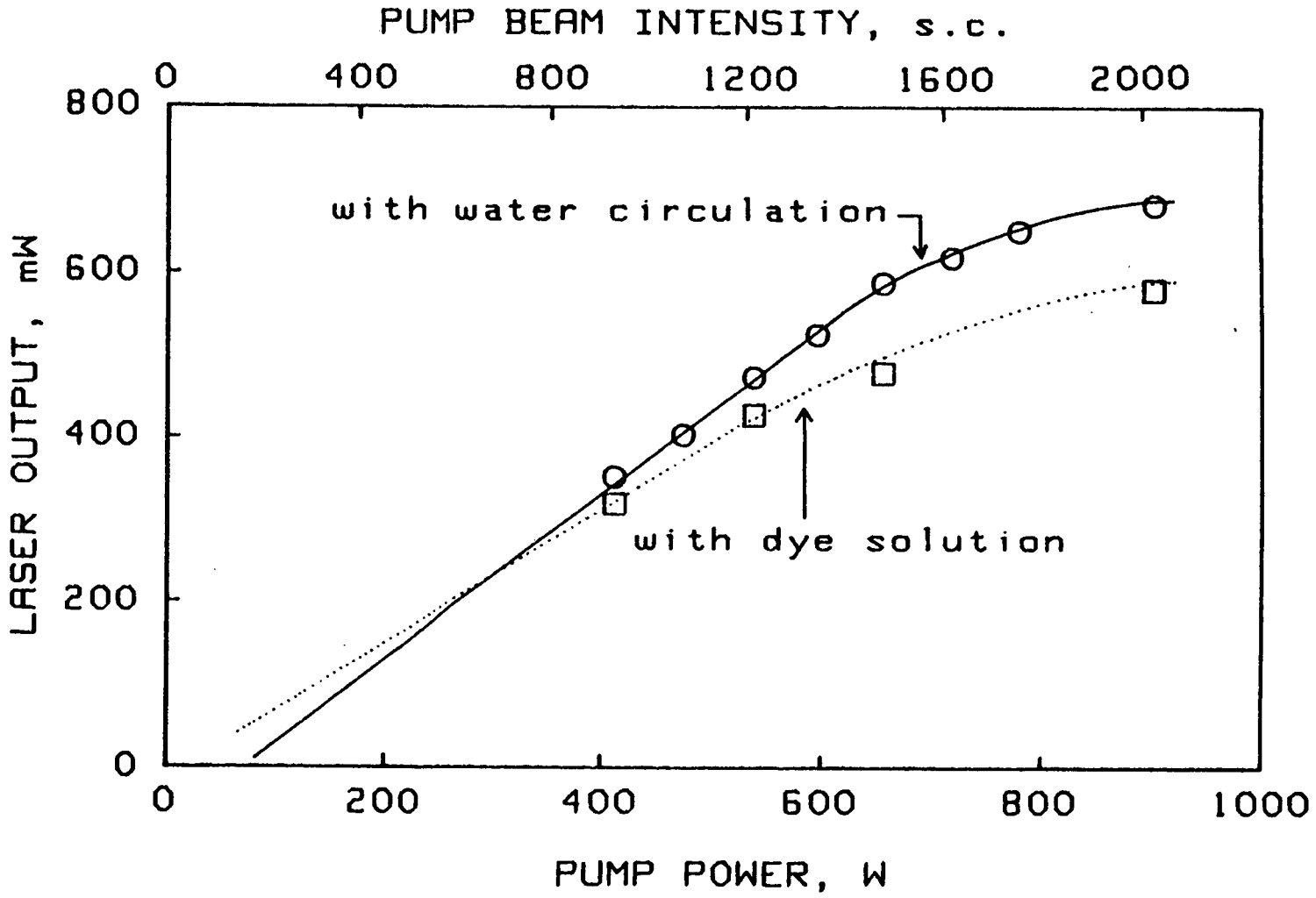

Figure 14. The CW laser output from a 1/8" diameter Nd:YLF rod as a function of pump power with water circulation and with dye circulation in the cooling jacket. The glass tube used in this measurement had 13 mm outer diameter and 11 mm inner diameter. See text for discussion on these data.

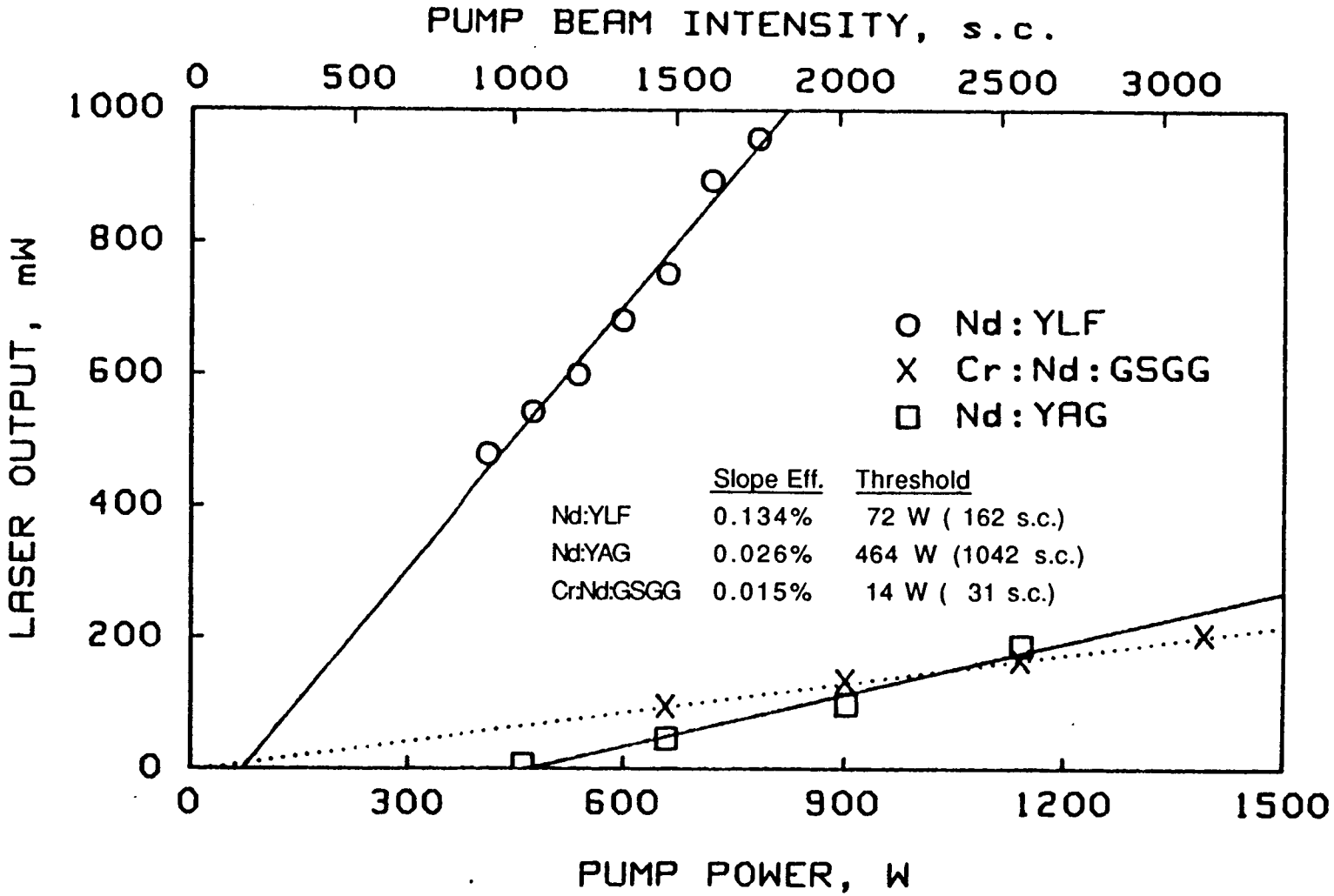

Figure 15. CW laser output powers of the Nd:YAG and Nd:YLF crystals and average power of the quasi-CW laser output of the Cr:Nd:GSGG crystal at various pump powers. Comparison among the crystals may not be made from this drawing. See text for reason. The size of each crystal rod was 1/8" thick and 3" long.

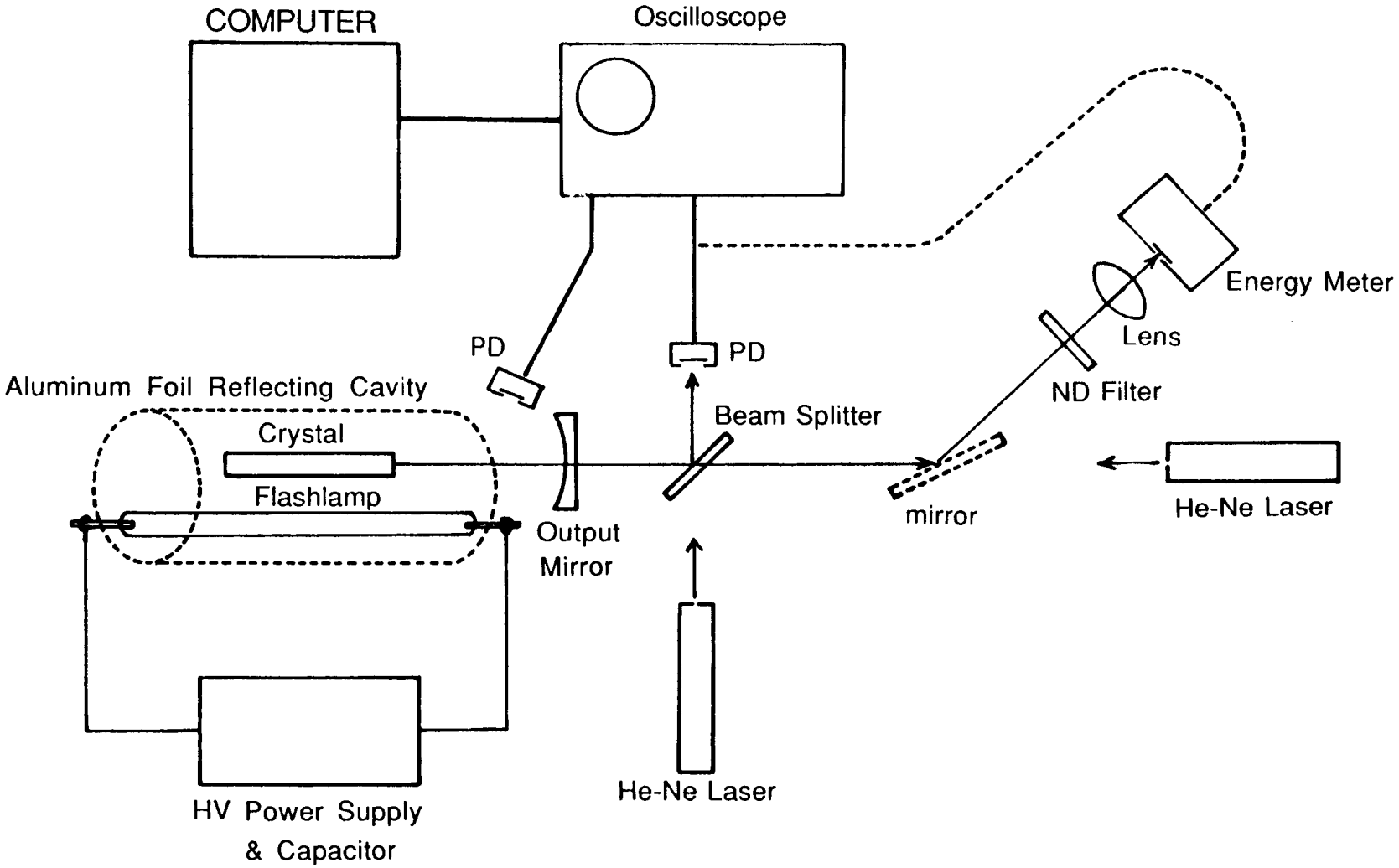

Figure 16. Experimental setup for flashlamp experiment. A 1.3 μF capacitor was used along with the power supply. PD: silicon photodiode, ND: neutral density filter and BS: beam splitter.

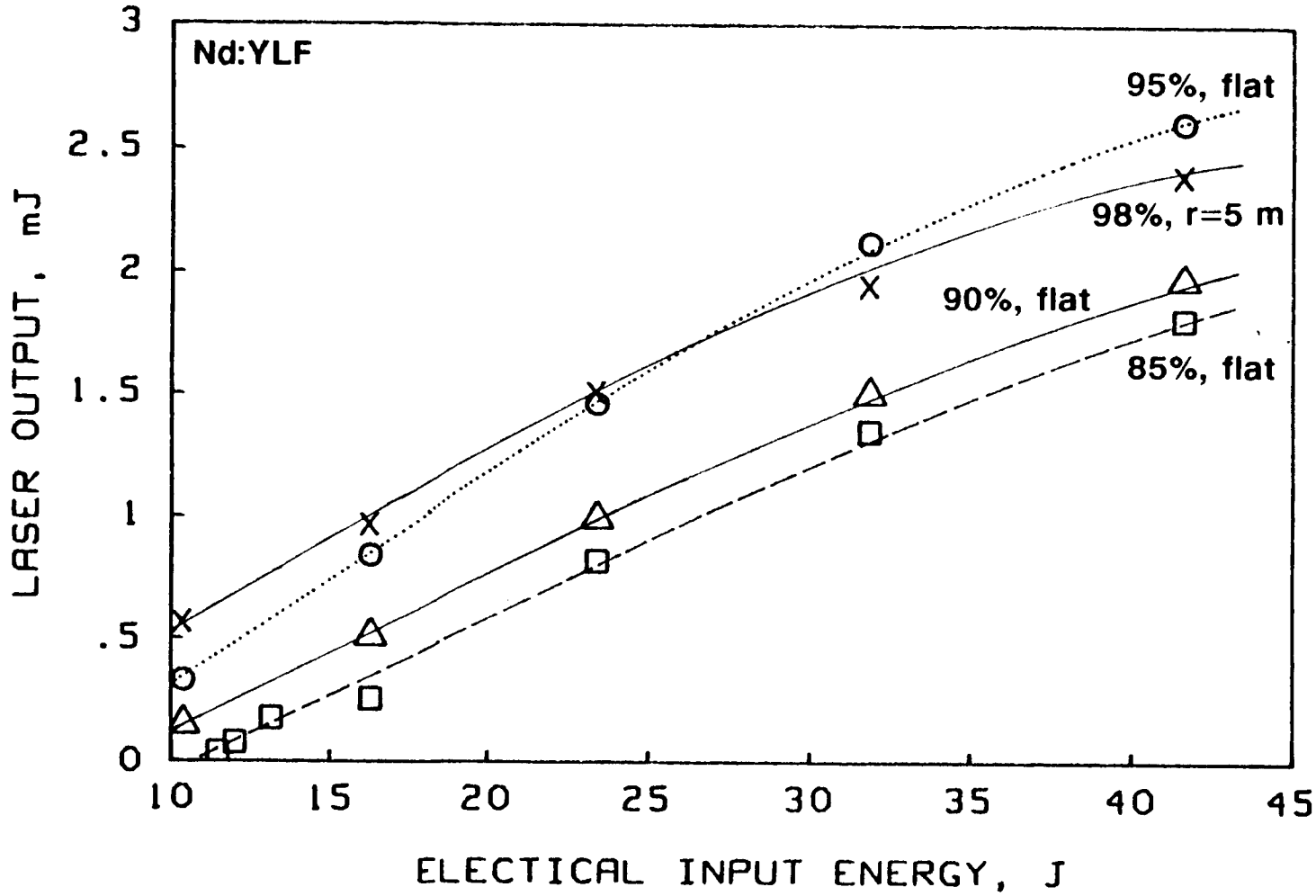

Figure 17. The output energy of the flashlamp-pumped Nd:YLF laser with various output coupling mirrors as a function of the electrical input energy.

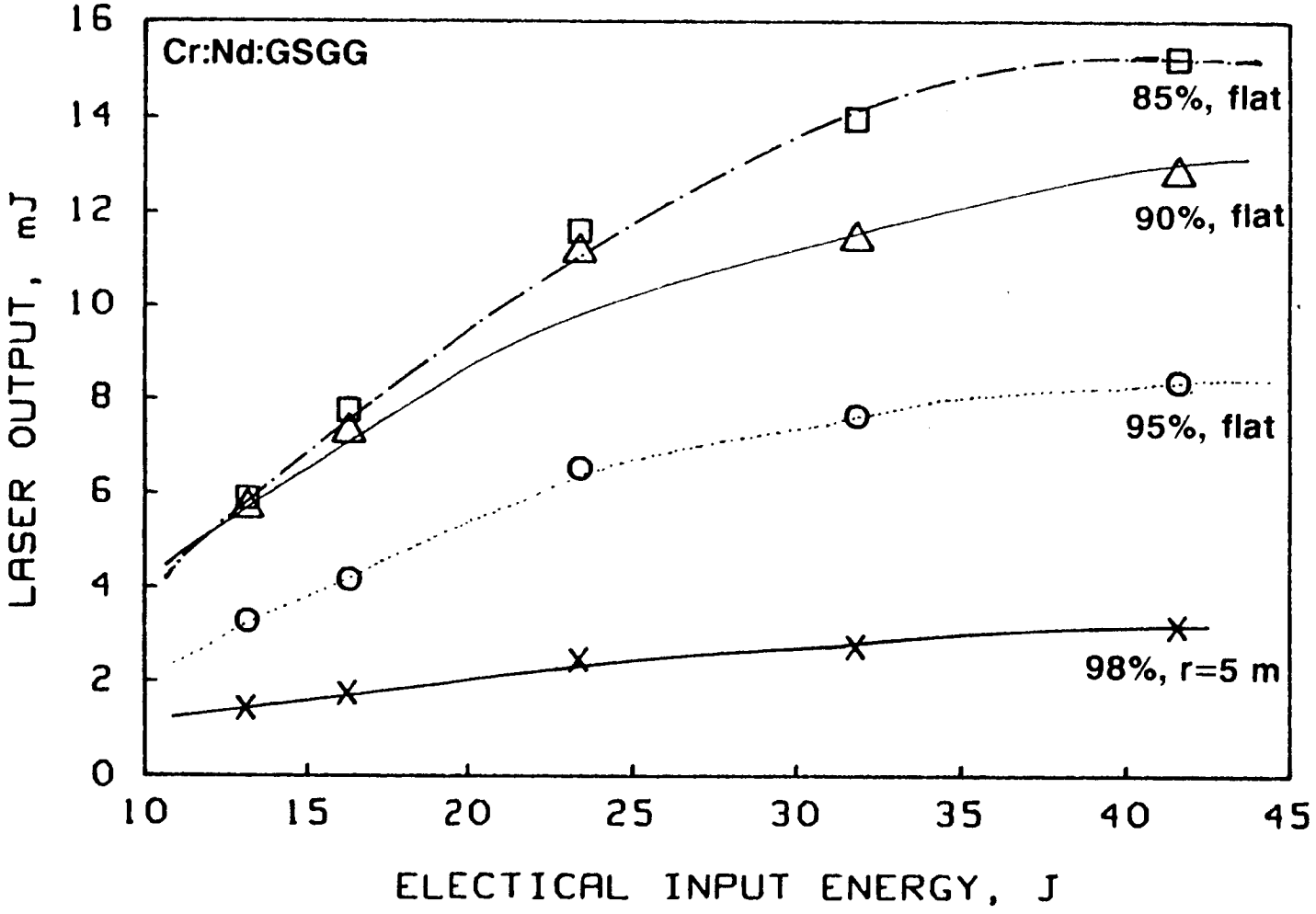

Figure 18. Flashlamp-pumped Cr:Nd:GSGG laser output with various output mirrors as a function of input energy. The scales are not comparable with the ones in Figs. 17 and 19 because the experimental condition was changed.

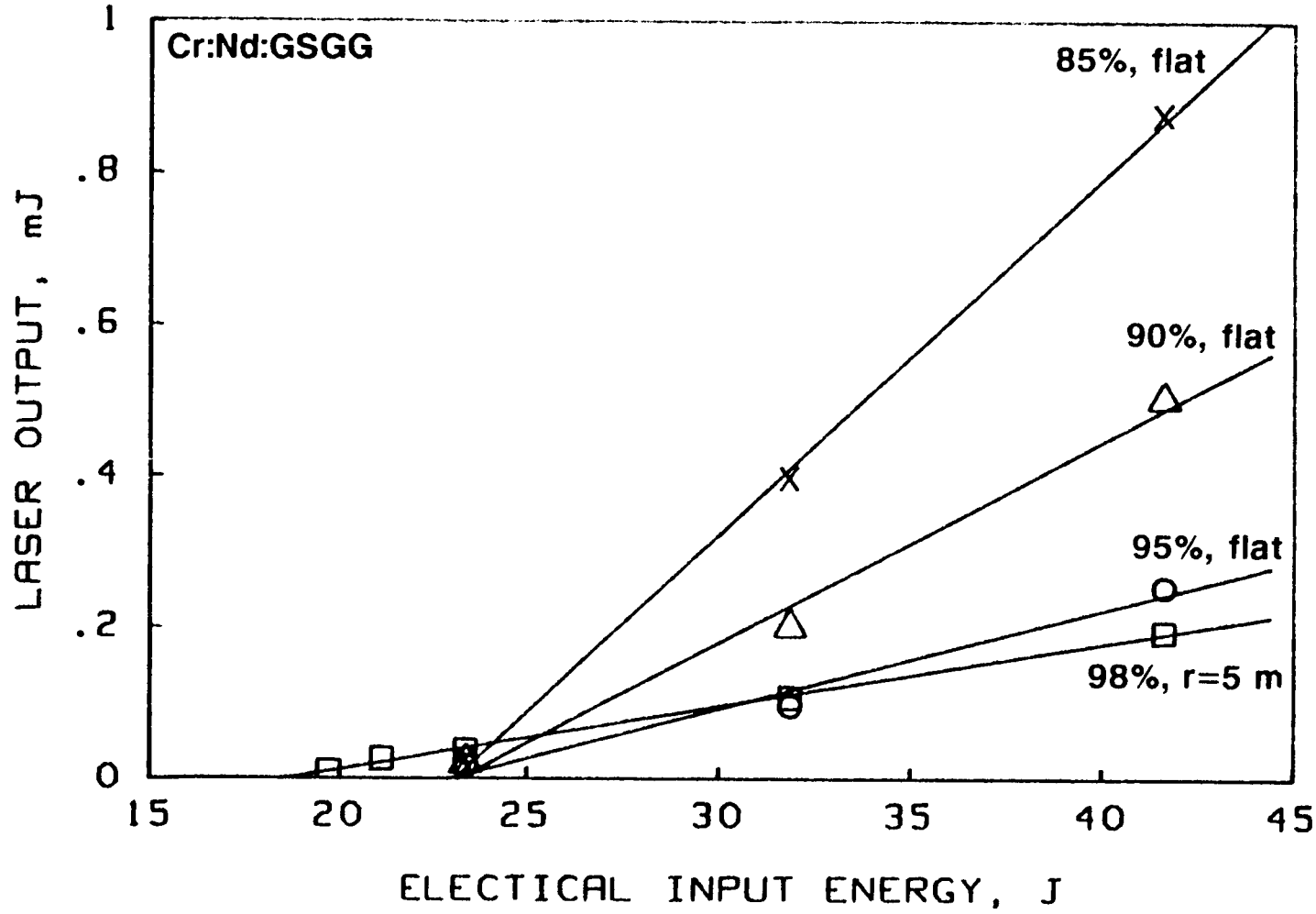

Figure 19. Flashlamp-pumped Cr:Nd:GSGG laser output with various output mirrors as a function of low input energy. The x-axis scale should not be compared with that in Fig. 18 because the experimental condition was changed.

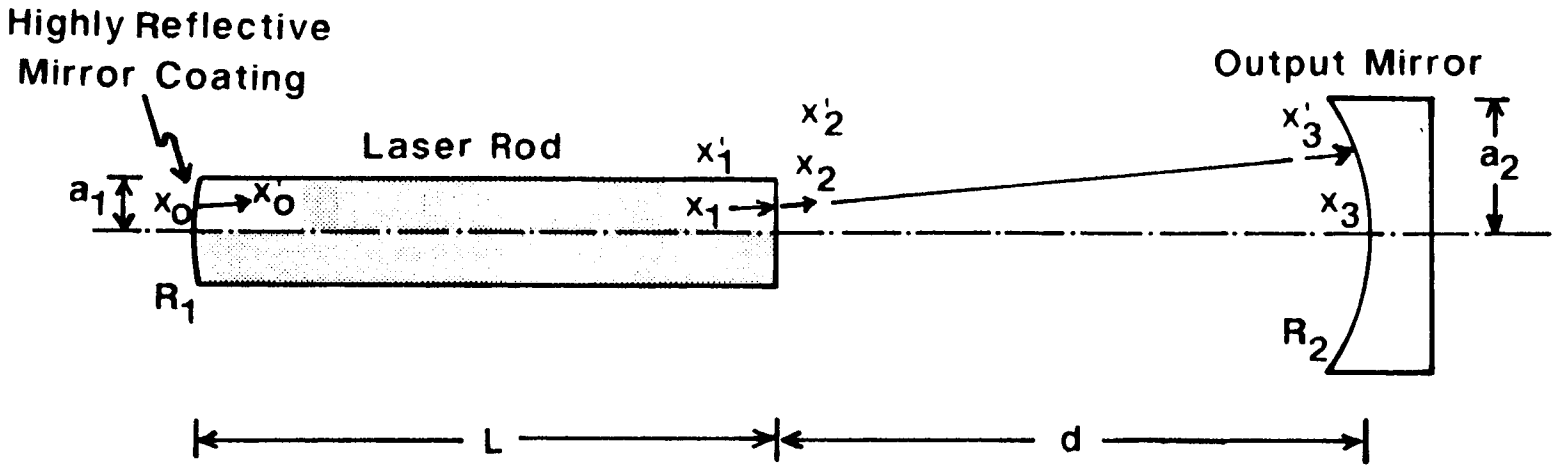

Figure 20. A diagram showing ray positions (x) and directions (x') with respect to the central axis line at various positions in the laser cavity used in our experiment 2a, and $2a_2$ are the diameters of the mirrors, and R_1 and R_2 are the radii of the mirror curvatures.

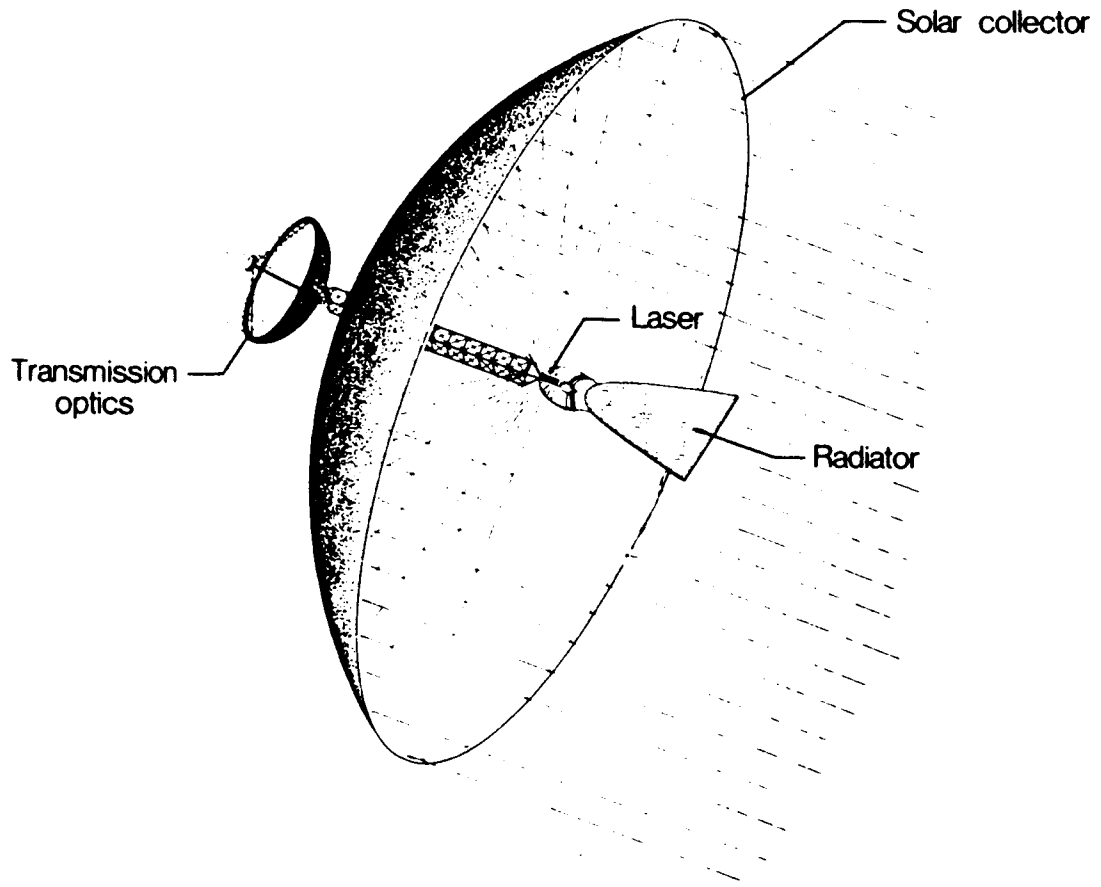

Figure 21. Solar-pumped laser system with a parabolic collector.

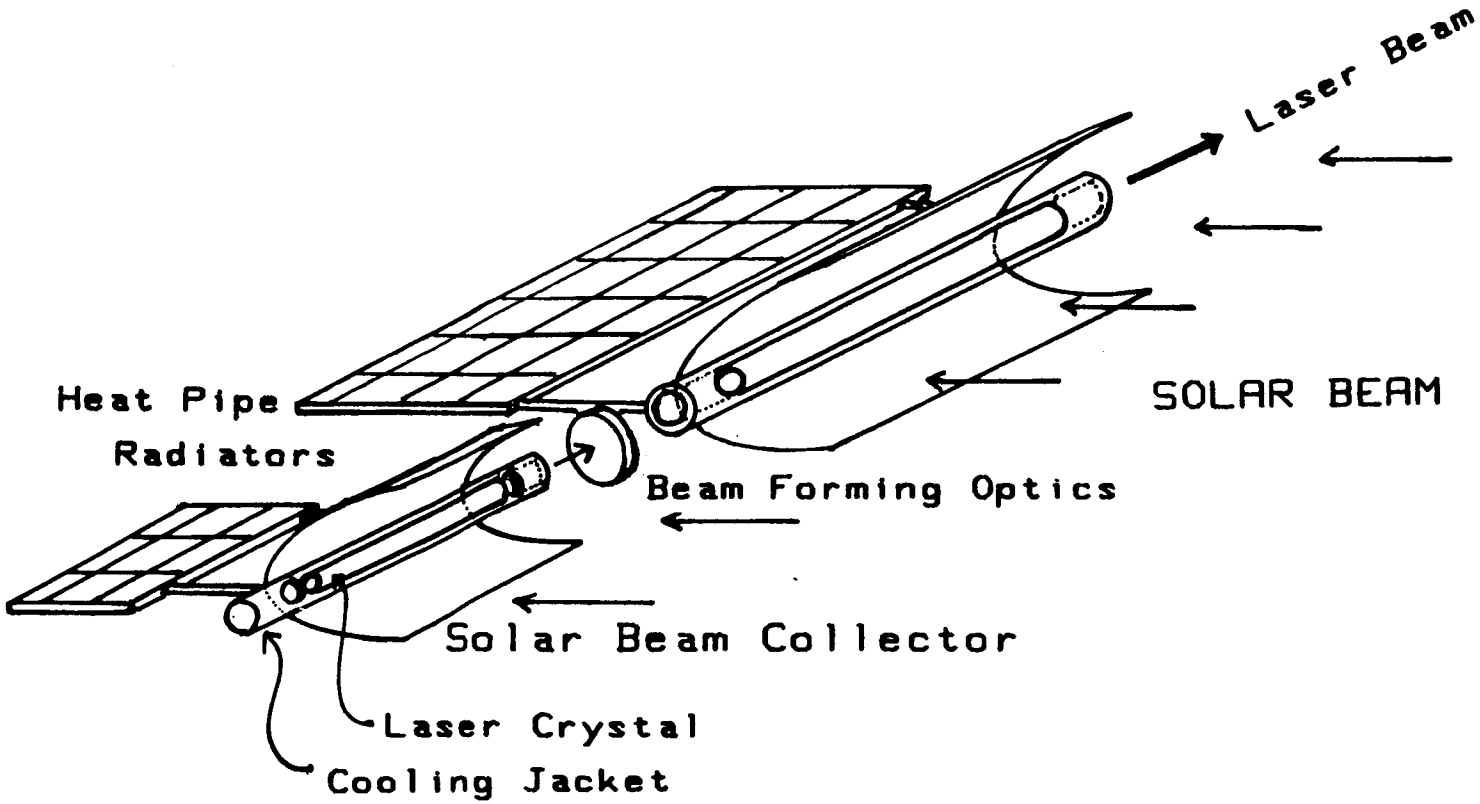

Figure 22. Solar-pumped laser-amplifier system with a trough type of collector.